Journal of Physics:
Condensed Matter

TOPICAL REVIEW • OPEN ACCESS

Shedding light on epitaxial SiGeSn alloys with Raman spectroscopy: local order and thermomechanical properties

To cite this article: Agnieszka Anna Corley-Wiciak *et al* 2025 *J. Phys.: Condens. Matter* **37** 493002

View the article online for updates and enhancements.

You may also like

- Magnetic circular dichroism at the oxygen K-edge in microcrystals of spinels grown on Ru(0001)
Anna Mandziak, Victor Sosa, Pawel Nita et al.

- Characterization of the mechanical properties of quasi-two-dimensional systems of rigid spheres
Y M Oliveira and L G Rizzi

- A map of cavity magnonics: concepts, developments, and recent advances
Rair Macêdo, Mawgan A Smith, Alban Joseph et al.

This content was downloaded from IP address 134.94.54.17 on 29/01/2026 at 14:40

OPEN ACCESS
IOP Publishing

Journal of Physics: Condensed Matter

J. Phys.: Condens. Matter **37** (2025) 493002 (23pp)

https://doi.org/10.1088/1361-648X/ae1c0b

Topical Review

Shedding light on epitaxial SiGeSn alloys with Raman spectroscopy: local order and thermomechanical properties

Agnieszka Anna Corley-Wiciak[1], Ignatii Zaitsev[2], Omar Concepción[3], Dan Buca[3], Costanza L Manganelli[2], Giovanni Capellini[2,4] and Davide Spirito[5,*]

[1] ESRF—European Synchrotron Radiation Facility, 71 avenue des Martyrs, CS 40220, 38043 Grenoble Cedex 9, France
[2] IHP—Leibniz Institute for High Performance Microelectronics, Frankfurt (Oder), Germany
[3] Peter Grünberg Institute 9 (PGI 9) and JARA-Fundamentals of Future Information Technologies, Forschungszentrum Jülich, Jülich, Germany
[4] Dipartimento di Scienze, Università Roma Tre, Roma, Italy
[5] BCMaterials, Basque Center for Materials, Applications and Nanostructures, UPV/EHU Science Park, 48940 Leioa, Spain

E-mail: davide.spirito@bcmaterials.net

Received 14 July 2025, revised 10 October 2025
Accepted for publication 5 November 2025
Published 3 December 2025

Abstract

Thanks to recent breakthroughs in their epitaxy compatible with industrial standard, (Si)GeSn alloys are now emerging as material platform for monolithic integration of next-generation electronics, optoelectronics, thermoelectrics, and photonics. In order to support the rapid evolution of the (Si)GeSn material system, different advanced characterization methods have to be developed to investigate its many interesting physical properties. This work provides an overview of Raman spectroscopy investigation of binary GeSn and ternary SiGeSn alloys. After reviewing the fundamental principles of Raman spectroscopy, the typical features of (Si)GeSn alloy Raman spectra are introduced. These features are then attributed to vibrational modes of atom pairs, high-order scattering, or disorder-induced scattering. The discussion also covers the details of polarization-resolved Raman spectroscopy applied specifically to the group-IV alloys case, with a focus on probing the local atomic ordering. Different applications of the Raman spectroscopy to the (Si)GeSn material system are covered. Initially, micro-Raman measurements are complemented by ancillary techniques, such as x-ray diffraction. This allows the spatially resolved composition and strain of the investigated epitaxial alloys to be determined based on calibrated coefficients of vibrational mode shifts. Raman hyperspectral imaging, along with its integration with numerical simulations for strain mapping in microstructures and devices, is also presented.

* Author to whom any correspondence should be addressed.

Original content from this work may be used under the terms of the Creative Commons Attribution 4.0 licence. Any further distribution of this work must maintain attribution to the author(s) and the title of the work, journal citation and DOI.

© 2025 The Author(s). Published by IOP Publishing Ltd

Subsequently, temperature-dependent Raman spectra are employed to investigate the crystal anharmonicity and the lattice expansion, with a detailed analysis of the multiple-phonon scattering coefficients, that are then compared with data present in the literature. The temperature dependence of Raman modes is also used to develop Raman thermometry to measure lattice thermal conductivity, in view of the recently proposed use of these materials in integrated opto–thermo-electronic devices. In summary, Raman spectroscopy is demonstrated as an essential tool for metrology and physical insight of the technologically relevant and complex SiGeSn ternary alloy system.

Keywords: SiGeSn, GeSn, Raman spectroscopy, metrology, polarized Raman spectroscopy, strain mapping, semiconductor alloys characterization

1. Introduction

Epitaxial semiconductor alloys are at the cornerstone of the electronic and photonic technologies. Controlling their physical properties, particularly the energy bandgap, by adjusting the composition and lattice parameters enables the engineering of materials for devices on demand. The development of alloys that can be integrated within the CMOS (Complementary Metal–Oxide–Semiconductor) technology manufacturing flow is especially important for enabling new functionalities to the Si-based microelectronic platform.

A major breakthrough in this area, particularly for the integrated photonics realm, has been the successful alloying of α-Sn with other group-IV materials, realizing binary (GeSn [1] and SiSn [2]), ternary (SiGeSn [3]), and even quaternary (CSiGeSn [4]) epitaxial alloys deposited on Si substrates. Incorporating the semi-metal α-Sn within a (Si)Ge matrix narrows both the (direct) bandgap at the Γ point and of the (indirect) bandgap at the L point of the Brillouin zone. The direct bandgap energy decreases at a higher rate with increasing Sn content x, compared to the indirect band gap. This leads to an indirect-to-direct transition for $x \sim 8$ at.% Sn for unstrained epitaxial layers [5, 6]. Ternary alloys with silicon further expand the ability to control the optical properties of epitaxial layers. They also enable the control of lattice parameter matching to the substrate, thus separately enabling the engineering of strain in electronic and optical properties [7–10]. These possibilities are particularly interesting for developing optoelectronic devices, since the directness of the band gap is associated with higher radiative recombination rate, enabling efficient charge to light or light to charge conversion in Si-based materials [6, 11].

To this aim, advancements in the epitaxial of (Si)GeSn alloys deposited on strain-controlled Ge/Si virtual substrates—especially by industry-standard chemical vapor deposition (CVD)-led to materials used to demonstrate different optoelectronic devices such photodetectors [12–14], photovoltaic cells [15, 16], light-emitting diodes [17, 18], and, ultimately, integrated lasers, both optically and electrically pumped [7, 19–22]. Fostered by the efforts deployed for developing optoelectronic devices, (Si)GeSn alloys made their way in other application domains. Indeed, the inclusion of Sn reduces the effective mass of electrons and holes, enhancing mobility in field-effect transistors [23–25], and enabling phase-coherent electron transport for quantum computing and spintronics [26]. Furthermore, the favorable electrical conductivity and Seebeck coefficients, combined with low lattice thermal conductivity due to alloy phonon scattering, open opportunities for thermoelectric applications [27–29].

However, developing such a high-quality material system proved to be a significant challenge. In fact, the inherently low solubility of Sn in Ge and Si, the substantial lattice mismatch between Sn and these host materials [6], and the poor thermal stability of Sn [30], all present major obstacles—particularly when relatively high Sn concentrations are needed for short-wave infrared (SWIR) and near-infrared (NIR) applications ($x > 10$ at.%). As a result, non-equilibrium growth conditions, such as low temperatures and high growth rates, are typically employed [5, 6].

At the same time, the study of the structural and optical properties revealed key differences from those of another group-IV alloy—SiGe, which has been well developed and investigated in the past years. Both Si and Ge have a diamond face-centered cubic crystal structure, with a moderate lattice mismatch of $\sim$4% and they are perfectly miscible across the composition range. Sn, instead, adopts a diamond structure below 13 °C in α-phase crystallization, with a considerable lattice mismatch of $\sim$15% with Ge, and transforms to a metallic β-phase at higher temperatures. Thus, the diamond structure alloy must compensate for the large mismatch, resulting in a limited range of Sn content in Ge, and in general, in a metastable structure. This also affects the ordering of the alloy. While SiGe is well-described by a random alloy model (i.e. there is no correlation between pairs of atoms), (Si)GeSn exhibits preferential atomic pairings that lead to inhomogeneity at the atomic scale, as shown by both numerical simulations [31–33] and experimental measurements [34–36]. At a fundamental level, specific alloy configurations, along with defects and disorder, may underlie the observed trends in optical properties [32, 37–39].

In light of these complex challenges, reliable, fast, and effective methods for investigating these materials are essential. Raman spectroscopy can provide characterization and insight into semiconductor properties, such as composition, strain, and disorder, by probing their vibrational modes. It is a lab-scale technique that requires minimal or no sample preparation and is non-destructive. It can be adapted for temperature and pressure-dependent measurements, and spatial mapping of the physical properties of materials or devices with sub-μm resolution. In developing Raman spectroscopy for (Si)GeSn materials, comparisons with well-studied SiGe alloys have served as a guideline. However, as mentioned before, the GeSn and SiGeSn have peculiar features, related to the poor solubility of Sn, that make the alloy qualitatively different from SiGe. The assignment of the experimental features to given Raman modes has also been under scrutiny because of the overlapping of the first and higher-order modes, and due to the unclear nature of some spectral features. In this work, various features of Raman spectroscopy for the characterization of SiGeSn alloys, addressing these challenges and exploring the potential of the technique, are presented.

In section 2, we introduce the principles of Raman spectroscopy for the case of group-IV semiconductors, also considering the details of polarization-related selection rules for the relevant symmetries. Then, we present the features of GeSn and SiGeSn spectra, their assignment to specific vibrational modes associated with atom pairs and disorder effects, primarily in epitaxial crystalline layers, with a brief note on amorphous and nanostructured materials. Section 4 showcases the short-range order and its analysis via polarized spectroscopy. Section 5 focuses on the main application of Raman spectroscopy in semiconductor metrology, particularly for determining composition and strain, and reviews the quantitative results from the literature. Section 6 presents the use of hyperspectral Raman mapping for the evaluation of strain distribution on micro-devices. Section 7 describes the effect of temperature on Raman spectra and the application for thermometry. We conclude by outlining the open questions and envisioning future directions for Raman-based characterization of group-IV semiconductor alloys.

2. Raman in group-IV semiconductors and alloys

Raman scattering is an inelastic light scattering process in which the incident light interacts with vibrational modes of the sample. As a result, the spectrum of the scattered light has components at the incident energy (elastic, Rayleigh scattering) and at lower (Stokes) and higher (Anti-Stokes) energies, respectively, with the elastic scattering being several orders of magnitude stronger. The energy separation between the elastic and inelastic peaks directly measures the energy of vibrational modes: as the energy is affected by material properties such as strain and composition, metrology of these quantities is possible [40, 41]. Modulation of mode intensity as a function of experimental conditions, e.g., temperature, scattering geometry, and light polarization, provides further information on the anharmonicity of the modes and on the symmetry of the crystals [42].

In crystals, the number of active Raman modes depends on the lattice symmetry (specifically, the point group) and the number and positions of atoms in the unit cell. The conditions for Raman scattering are primarily governed by energy and momentum conservation laws, expressed as:

$$\omega_s = \omega_i \pm \omega_p, \ \overrightarrow{k_s} = \overrightarrow{k_i} + \overrightarrow{k_p} \tag{1}$$

where the subscripts $s, i,$ and p refer to the scattered light, incident light, and phonon, respectively. However, considering the negligible momentum of the photons with respect to the typical Brillouin zone (BZ) extension, only phonons with finite energy at the BZ center Γ can be involved in first-order Raman scattering, due to momentum conservation $k_i \sim k_s \sim k_p \sim 0$. Additional Raman peaks will appear in the spectra because of high-order scattering as a combination of modes far from the zone center (see figure 1(a)) [43, 44].

Then, the classical scattered intensity for first-order Stokes scattering is given by [40, 41]

$$\frac{\partial \sigma}{\partial \Omega} \propto \omega_s^4 \left| \widehat{e_i}^T \frac{\partial \chi}{\partial \boldsymbol{Q}} \boldsymbol{Q}(\omega_i) \widehat{e_s} \right|^2 (n_p + 1) \tag{2}$$

where $e_{i,s}$ are the polarization unit vectors of the incoming and scattered radiation, Q is the atomic displacement due to the phonon mode, χ is the dielectric susceptibility tensor, and n_p the Bose–Einstein occupancy for the phonons. The term $\frac{\partial \chi}{\partial \boldsymbol{Q}} \boldsymbol{Q}(\omega_0) = \overleftrightarrow{R}$ is called Raman tensor.

The important features of this result are the role of light polarization and its interplay with the Raman tensor, which is discussed in more detail below, and the power law for the optical frequency. The scattering intensity is proportional to ω^4 (λ^{-4} in terms of wavelength), that is, UV and blue light are more efficient with respect to red and NIR.

The quantum perturbation theory can be used to derive the Raman tensor as well, referring to the electronic transitions associated with absorption and emission of photons and electron–phonon interaction. The leading term for the cross-section is [40]

$$\frac{\partial \sigma}{\partial \Omega} \propto \left| \sum_{n,n'} \frac{\langle 0|\mathcal{H}_e(\omega_s)|n'\rangle \langle n'|\mathcal{H}_{\mathrm{ep}}|n\rangle \langle n|\mathcal{H}_e(\omega_i)|0\rangle}{[\hbar\omega_i - (E_n - E_0)][\hbar\omega_i - \hbar\omega_p - (E_{n'} - E_0)]} \right|^2 \tag{3}$$

where $\mathcal{H}_e$ is the electron-radiation Hamiltonian and $\mathcal{H}_{\mathrm{ep}}$ the electron–phonon Hamiltonian; the initial electronic state with energy E_0 is labeled as '0', and n,n' are intermediate electronic states.

This equation also shows that for incident (or scattered) light matching an electronic transition $(E_n - E_0)$, a resonant

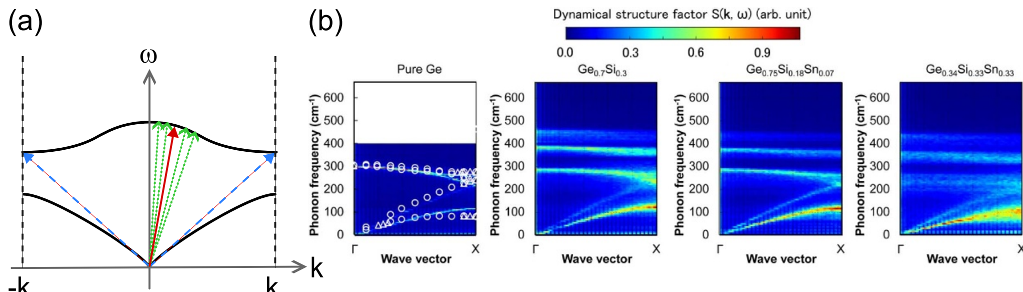

Figure 1. (a) Sketch of a phonon dispersion showing an optical and an acoustic branch. The arrows represent the scattering process involved in Raman scattering. Red, continuous line: first order scattering, at zone center (the deviation from zone center is exaggerated for clarity); blue, dashed lines: second order scattering at zone boundary; green, dotted lines: disorder activated scattering probing the phonons near the zone center. (b) Phonon dispersions for Ge, $Ge_{0.7}Si_{0.3}$, $Si_{0.18}Ge_{0.75}Sn_{0.07}$, and $Si_{0.33}$ $Ge_{0.34}Sn_{0.33}$, obtained by calculation of the dynamical structure factor by molecular dynamics (b). Reproduced from [47]. © 2018 The Japan Society of Applied Physics. All rights reserved.

enhancement can be obtained. For the case of GeSn, a useful resonance is found in the vicinity of the E_1 gap, close to an excitation with a wavelength of 633 nm [45, 46].

To discuss the selection rules for Raman spectroscopy with polarized light, we consider that each vibrational mode in a crystal belongs to an irreducible representation of the point group of the lattice. In the case of group-IV semiconductors with diamond crystal structure (e.g. Si, Ge), with point group O_h, the phonon spectrum has three acoustic modes and three optical modes. The latter belongs to the T_{2g} representation, 3-fold degenerate at the Γ point of the BZ. The first-order Raman spectrum of crystalline Ge or Si thus features a single main peak ($\omega_{\mathrm{Ge-Ge}}$ ∼300 cm^{-1} in Ge) corresponding to the zone-center optical phonons. Other peaks (∼150 cm^{-1}, 600 cm^{-1} in Ge) are associated with second-order scattering of acoustic and optical phonons, and may follow different polarization dependence.

Raman spectra of binary alloys, such as GeSn and SiGe, or ternary SiGeSn, are instead qualitatively different from those of the elemental semiconductor. The presence of multiple atomic species (e.g. Si and Ge in $Si_{1-y}Ge_y$) gives rise to modes associated with specific atomic pair vibrations: Si–Si, Ge–Ge, and Si–Ge. Those modes appear at energies close to the optical phonon energy of pure constituent—Si or Ge and intermediate values, respectively. Their exact energy depends on the composition y, and can thus be used for metrology [48]. The relative intensity of the peaks may also be matched to the number of pairs of each type, in the hypothesis that the cross section is the same for all modes. Figure 1(b) shows the result of molecular dynamics simulations for the dispersion of phonons in pure Ge and in exemplary SiGe and SiGeSn alloys. The bands observed at phonon frequencies nearly constant throughout the BZ correspond to the optical phonon branches that can be observed by first-order Raman scattering, and in particular to Si–Si (∼450 cm^{-1}), Si–Ge (∼400 cm^{-1}), and Ge–Ge (∼300 cm^{-1}), respectively.

The selection rules are weakened in the presence of disorder or deformation in the lattice. Unlike pure crystals, alloys do not exhibit perfect translational symmetry because of the random location of the atomic species. In $Si_{1-y}Ge_y$, although the diamond lattice is preserved with well-defined atomic sites, those sites are randomly occupied by either Si or Ge atoms. Nonetheless, this random substitution leads to mass disorder and local strain fields due to differences in atomic mass and bonding strength, which in turn affect physical properties such as thermal conductivity [49, 50]. In Raman spectra, this disorder causes asymmetric peak broadening and the appearance of additional spectral features, such as broad bands or shoulders [51]. These features appear because of the relaxation of the momentum conservation rule brought about by the loss of ideal translational symmetry of the alloy lattice. In fact, the defect can be seen as a source of infinite momentum, which activates the scattering from all the phonon modes matching the scattering energy, as sketched in figure 1(a), so that the Raman spectrum samples the phonon density of states.

Nonetheless, despite the structural and compositional complexity, it is often useful to approximate the alloy system using the same point group and representation as the corresponding pure materials. While this approximation is not strictly valid, it serves as a practical guideline for interpreting Raman spectra by identifying modes and understanding their origin, as discussed in more detail in the following.

2.1. Polarized Raman spectroscopy and selection rules

Raman selection rules are derived from the symmetry of the crystal, in particular from its point group and the arrangement of atoms in the unit cell, which yield the symmetry of the resulting vibrational modes. Raman intensity is given by the equations (2) or (3), using the form $I \propto |\widehat{e_i^T}\overleftrightarrow{R}\widehat{e_s}|^2$, where $e_{i,s}$ are the polarization unit vectors of the incoming and scattered light and R is the Raman tensor, respectively.

Each vibrational mode belongs to one of the irreducible representations of the point group, which thus determines the form of the Raman tensor. For the point group O_h, which is strictly appropriate to describe the diamond lattices of the elemental semiconductors, the Raman active representations are

Table 1. Polarization configurations and active representations for incidence along z = ⟨001⟩.

Porto notation	Active representations
$z(x'x')\bar{z}$ 'allowed'	$A_{1g}+E_g+T_{2g}$
$z(y'x')\bar{z}$ 'forbidden'	E_g
$z(xx)\bar{z}$ 'forbidden'	$A_{1g}+E_g$
$z(yx)\bar{z}$ 'allowed'	T_{2g}

A_{1g}, E_g, and T_{2g}; their Raman tensors are [52]

$$R(A_{1g}) = a\begin{pmatrix}1&0&0\\0&1&0\\0&0&1\end{pmatrix}, R\left(E_g^{(1)}\right) = b\begin{pmatrix}1&0&0\\0&1&0\\0&0&-2\end{pmatrix},$$
$$R\left(E_g^{(2)}\right) = \sqrt{3}b\begin{pmatrix}-1&0&0\\0&1&0\\0&0&0\end{pmatrix}, R\left(T_{2g}^{(x)}\right) = d\begin{pmatrix}0&0&0\\0&0&1\\0&1&0\end{pmatrix},$$
$$R\left(T_{2g}^{(y)}\right) = d\begin{pmatrix}0&0&1\\0&0&0\\1&0&0\end{pmatrix}, R\left(T_{2g}^{(z)}\right) = d\begin{pmatrix}0&1&0\\1&0&0\\0&0&0\end{pmatrix}. \quad (4)$$

Here, the reference frame is aligned with the [100], [010], [001] crystal directions. For the degenerate representations, the intensity is calculated for each member and then added (incoherent combination). Each representation depends only on a single free parameter (*a, b, d*, respectively). Thus, the selection rules (presence/absence of a peak in a specific polarization and relative orientation of polarization and crystal axes) and the intensity angular pattern (by rotating the polarization or the sample) are independent of the value of the coefficient, which instead may be calculated from the scattering cross section.

Many reported experiments are performed in few selected configurations, which are typically indicated using the so-called Porto notation as $k_i(e_i\ e_s)k_s$, with $k_{i,s}$ the incidence and scattering direction. Incidence direction and polarization are usually aligned with high-symmetry directions, labeled as z = [001], x = [100], y = [010], x' = [110], y' = [1$\bar{1}$0], as sketched in figure 2(a).

In a typical case, epitaxial wafers or chips are grown along the ⟨001⟩ direction; the cleaving direction in this case is the ⟨110⟩, enabling an easy identification of crystal axes and a 'natural' reference system when wafer coupons are used for the measurements. In advanced micro-Raman setups, the measurements are conducted in backscattering geometry, with k_i and k_s vectors being antiparallel and often along the z = ⟨001⟩ direction.

In this case, the active representations in the four typical configurations are listed in table 1. Considering the atomic positions in the diamond lattice, the only active mode for group-IV materials belongs to the T_{2g} representation. Thus, the setting when this representation is active is customarily indicated as 'allowed', while the others are 'forbidden'.

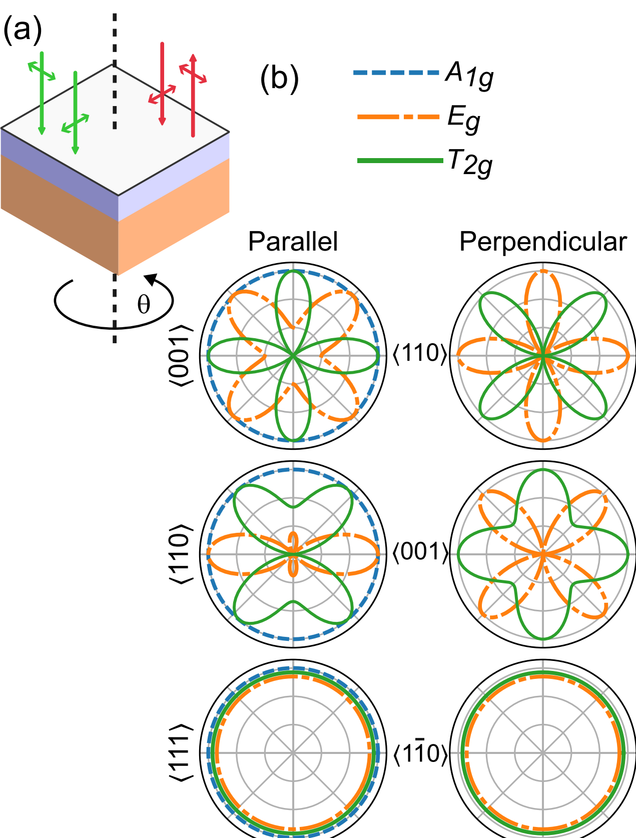

Figure 2. (a) Scheme of sample rotation for polarized experiments, in backscattering configuration. Incident and scattered light can have different polarizations. (b) Angular patterns of the irreducible representations of the O_h point group (A_{1g}, blue dashed line; E_g, orange dash-dot line; T_{2g} green solid line), as a function of the azimuth θ. Three incidence directions are considered for parallel and perpendicular alignment of the polarizers. For the ⟨111⟩ incidence, the three representations give the same constant pattern in parallel alignment, while in perpendicular E_g and T_{2g} are both constant, while A_{1g} is zero. The patterns are normalized to the maximum value.

When the spectra are acquired as a function of the azimuth angle (equivalently by rotating the sample or the polarization of incoming and scattered light [53]), characteristic patterns can be observed in crystalline, oriented samples, that depend also on the respective alignment (parallel or perpendicular) of the excitation and of the analyzer at the sensor entrance. These patterns are reported in figure 2(b) and table 2 for each mode for the cases of incidence along ⟨001⟩, ⟨110⟩, and ⟨111⟩.

The main T_{2g} peak, for example, when measured with incidence in the ⟨001⟩ direction, has a maximum intensity when both incident and scattered light are polarized along the ⟨110⟩ axes, while (ideally) disappears for alignment at ⟨100⟩, showing a characteristic quadrupolar pattern (figure 2(b)). Deviation from this pattern points to the role of disorder. In the extreme case of a completely disordered sample, an integral over the possible orientations, analogous to a liquid or powder sample, can be envisaged. In this case, angular dependence

Table 2. Azimuth dependence of polarized Raman scattering for each active mode of the O_h point group. The values are normalized to the maximum. For degenerate E_g and T_{2g} representations, the members are summed incoherently (i.e., we report the sum of the intensity of all the members).

Alignment	Repr.	Parallel	Perpendicular
$\langle 001\rangle$ $\theta = 0°$: [110]	A_{1g}	1	0
	E_g	$(1 + 2\sin^2(2\theta))/3$	$\cos^2(2\theta)$
	T_{2g}	$\cos^2(2\theta)$	$\sin^2(2\theta)$
$\langle 110\rangle$ $\theta = 0°$: [001]	A_{1g}	1	0
	E_g	$(3\sin^2(\theta)-2)^2/4$	$\sin^2(2\theta)$
	T_{2g}	$(5/9)\sin^2(\theta)\ (6–5\sin^2(\theta))$	$2\sin^4(\theta)-2\sin^2(\theta) + 1$
$\langle 111\rangle$ $\theta = 0°$: $[1\bar{1}0]$	A_{1g}	1	0
	E_g	1	1
	T_{2g}	1	1

does not provide information, and a constant dichroic ratio is measured.

Focusing on the T_{2g} symmetry of the first-order modes in diamond-like structures, we note that the three degenerate members do not have, in general, the same selection rule or angular pattern. For example, for the $\langle 001\rangle$ incidence, only one component is active (the LO mode).

A non-perfect selection rule can be also assigned to slightly misaligned samples (incidence is titled from the $\langle 001\rangle$ direction), especially in strained samples, where the reduction of symmetry breaks the 3-fold degeneracy and shifts the peak energy [54]. Still, only the LO mode is observed in the $\langle 001\rangle$ alignment. The split components can then be observed by slightly tilting the sample, or by use of high numerical aperture optics [55, 56], such as an oil-immersion objective [57].

The theoretical framework presented above has been extensively applied to the study of Raman spectra in group-IV alloys, enabling tagging of spectral features to specific vibrations by comparing their angular pattern. The presence of peaks associated with alloy components is then applied to the quantification of composition as well as strain in epitaxial layer. These developments are discussed in the next sections.

2.2. Experimental equipment and parameters

The key component in a Raman experiment is a spectrometer with high resolution and very high rejection of the elastically scattered light. This is obtained with multi-stage spectrometers (2 or 3 stages), or employing high-efficiency notch or bandpass filters, for example volume Bragg gratings, that may enable measurements at very low ($<$10 cm^{-1}). For high-quality crystalline materials such as pure Si or Ge, Raman peaks can be as narrow as 3 cm^{-1}, in contrast, alloys often have broader spectral features. To accurately deconvolute peaks and extract quantitative information (as discussed in section 3), high spectral resolution, ideally below 1 cm^{-1}, is essential. This depends on the geometry of the optical system, the wavelength, and the density of the lines in the dispersive grating. For the visible range, gratings with 3000 lines mm^{-1} are commonly employed. It is important to note that the resolution in terms of 'data points per cm^{-1}' may be different from the actual resolution of the instrument, due to oversampling [58].

The excitation wavelength λ is also a key parameter. As mentioned above, the Raman intensity is proportional to λ^{-4}, thus, short wavelengths (UV-blue) may be expected to greatly enhance the signal. However, short wavelengths are also highly absorbed in the opaque group-IV materials. Considering that the light enters and exits the sample in the typical backscattering geometry, the penetration depth can be estimated as $d \sim 1/(2\alpha)$ for a 1/*e* damping, α being the absorption coefficient at the excitation wavelength. Taking its value for Ge [59], excitation with 405, 532, 633, 785 nm yields a depth $d \sim 7$, 9, 30, 90 nm, respectively. Therefore, the visible spectrum represents a good trade-off between signal strength and probing depth.

The Raman spectra are often acquired using a microscope setup, whose optics give large laser power density for a high signal-to-noise ratio and enable mapping and space-resolved experiments. Polarized spectroscopy requires additional components, such as polarizers, waveplates, and rotational stages. A convenient setup involves rotating a half-wave plate placed before the objective, enabling angular-resolved spectroscopy without moving the sample. This ensures consistent probing of the same sample region. Alternatively, the sample itself may be rotated under fixed polarization conditions [53].

3. Raman spectra of (Si)GeSn alloys

In this section, we will describe the features observed in Raman spectra of GeSn and SiGeSn. We consider the case of high-quality, epitaxial layers of interest for applications in electronics and photonics, and of amorphous and nanocrystalline samples, which present specific features. Peaks associated with first-order Raman scattering from atom pair vibrations are expected and have been identified in the literature. Further peaks and shoulders are associated with alloy disorder and higher-order scattering, as discussed in section 4. The quantitative characteristics of the spectra, which can be used in material characterization, are discussed in detail in section 5.

3.1. Epitaxial GeSn and SiGeSn

In the early works of D'Costa *et al* [45, 60], the main features of the GeSn Raman spectrum were identified in a sample with up to 16% Sn. The spectra comprised a main peak near 300 cm^{-1}, associated with Ge–Ge pair vibration, with a characteristic asymmetric shape due to the relaxation of the wavevector conservation in the alloy. At lower Raman shift values, a peak at ∼255 cm^{-1} was attributed to Ge–Sn pair vibration, while a rather broad spectral feature on the low energy tail of the main peak, featuring a relative high intensity in 'forbidden' polarization, was assigned to disorder-assisted scattering (DA).

Further to lower energy (175 cm^{-1}), a peak that could potentially be assigned to the Sn–Sn vibration, based on the comparison with α-Sn which has a peak 197 cm^{-1}, has a debatable attribution, noted that it preserved a relatively high intensity also in 'forbidden' polarization configuration and that it overlaps with the second order LA phonon of Ge.

Subsequent studies tagged these peaks in high-quality, high-Ge content samples. The nature of the DA and 'Sn–Sn' modes was settled with further studies and comparison of polarization-dependent measurements and dependence on composition [8, 61, 62].

Ternary SiGeSn alloys have additional features related to Si atoms. Figure 3 reports spectra from a series of samples with ∼85 at.% Ge in SiGe, GeSn, and SiGeSn alloys, compared to in bulk Ge, to illustrate the evolution of the spectra with the composition and highlight the several spectral features [42].

In all samples, the strongest peaks are observed in the 'allowed' polarization configuration (top panel of figure 3), indicating that they preserve the first-order nature of the diamond lattice symmetry group despite the alloying. Given the relative abundance of Ge in all the samples the main peak is always found at ∼300 cm^{-1}, and is associated with Ge–Ge pairs vibrations. This is the only peak in the Ge sample and allows for the identification of the secondary modes (overtone and combinations), which are weak in the 'allowed' configuration (see middle panel of figure 3, that show the low-intensity region) and are stronger in the 'forbidden' configuration relative to the Ge–Ge peak. In particular, we observe two 2TA at ∼160 cm^{-1} and ∼230 cm^{-1}, a peak at ∼190 cm^{-1}, TO + TA at 355 cm^{-1}, the 2LA at 380 cm^{-1}, and three modes overlapping 2TO in the range 540 cm^{-1}–600 cm^{-1} [8, 60]. Assigning these modes allows a robust identification of the modes in the alloy when modes associated with the various atom pairs are present.

In SiGe alloy (15.0 at.% Si), two Si–Ge modes are found at ∼400 cm^{-1}, and two Si–Si modes at ∼430 cm^{-1} and ∼450 cm^{-1} [63–65], as visible in 'allowed' configuration. The Ge–Ge peak has a shoulder, stronger in the 'forbidden' case, at ∼290 cm^{-1}, associated with the DA modes in the phonon density of states. Similarly, in GeSn (14.9 at.% Sn), the Ge–Sn pair vibration is at 260 cm^{-1}, and the Ge–Ge has the DA shoulder. The mode around 175 cm^{-1}, as already observed by D'Costa *et al* [60], is strong in both 'allowed' and 'forbidden' configurations, supporting its attribution to a mixture of overtone 2TA of Ge and Sn–Sn [61].

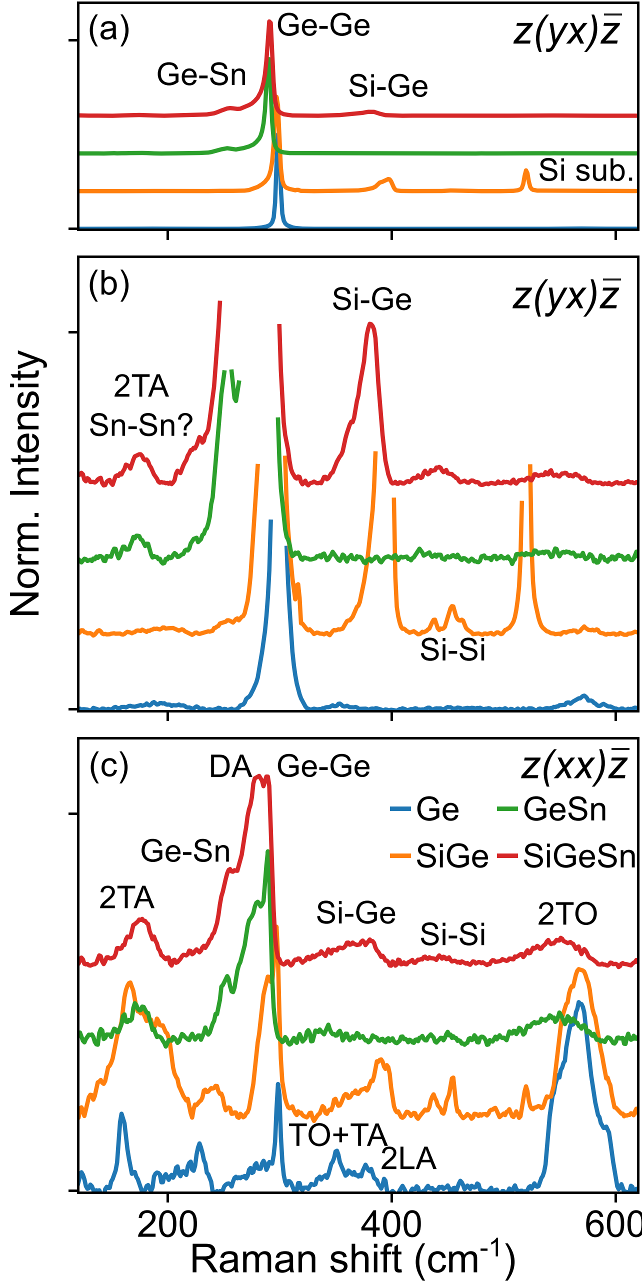

Figure 3. Raman spectra in different polarization configurations for pure Ge wafer, $Si_{0.15}Ge_{0.85}$, $Ge_{0.851}Sn_{0.149}$, and $Si_{0.021}Ge_{0.818}Sn_{0.161}$ epitaxial layers on Ge/Si. (a,b) 'Allowed' $z(yx)\bar{z}$ configuration (only T_{2g}-LO modes allowed); panel (b) is a zoom of the top. (c) 'forbidden' case (only A_{1g} + E_g modes allowed). Each spectrum is normalized to the Ge–Ge peak maximum. Data are derived from [42].

The intriguing DA shoulder has been subject to further studies, as discussed in [61]. It was found that DA could be decomposed into two components, very close in energy, one being active in the 'allowed' configuration, while the other

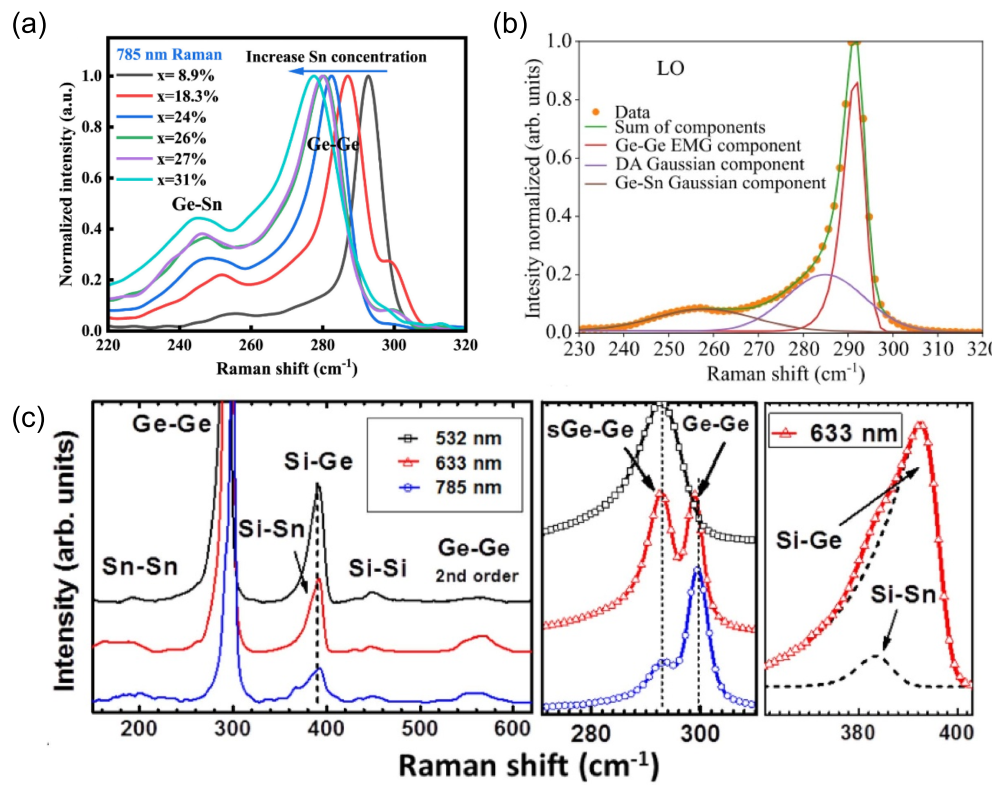

Figure 4. (a) Raman spectra of GeSn alloys up to 31% Sn, measured at 785 nm. (a) Reprinted from [67], Copyright (2024), with permission from Elsevier. (b) Raman spectrum of $Si_{0.021}Ge_{0.818}Sn_{0.161}$/Ge/Si sample acquired with 633 nm excitation in $z(yx)\bar{z}$ polarization, overlapped with results of fitting with an EMG (Ge–Ge) and two Gaussian peaks (DA and Ge–Sn). (b) Reprinted with permission from [42], Copyright (2024) by the American Physical Society. (c) Spectra from $Si_{0.04}Ge_{0.84}Sn_{0.12}$/Ge/Si acquired with different excitation wavelengths. The insets show the spectra ranges around Ge–Ge and Si–Ge modes. (c) Reprinted from [70], with the permission of AIP Publishing.

in the 'forbidden' configuration. The latter is associated with disorder, while the former is associated with the local ordering of Sn atoms in the alloy (for a detailed discussion of this topic, we refer the reader to section 4). At high Sn content, the disorder induces a consistent broadening of the peaks. Due to the limited solubility of Sn in Ge, high-quality binary GeSn samples with high Sn content require specialized growth techniques. Xu *et al* [66] use low-temperature CVD to achieve up to 27% Sn on Si substrates, observing increasing peak broadening and shifts with Sn content. Zhao *et al* [67] employ low-temperature molecular beam epitaxy (MBE) to fabricate GeSn with up to 31% Sn (figure 4(a)). They also observe a broadening and shift of the main peak (analyzed as a single feature) and an increase of the Ge–Sn peak with Sn content.

The peaks of the binary alloy are also found in the ternary SiGeSn system (10.8 at.% Si, 7.5 at.% Sn) [45, 63, 68, 69], and partially overlap with secondary modes. Si–Ge peak and secondary Ge peaks are overlapped, and differently from binary SiGe, there is only one peak for Si–Ge and Si–Si, the latter having a broad band at 400 cm^{-1}–500 cm^{-1}. The 2TA mode, similar to the GeSn case, appears as one peak. Sn–Sn is also overlapped with the 2TA, as evident in 'forbidden' configuration. In this sample, no peaks can be associated with Si–Sn, likely due to the low content of Si and Sn. D'Costa *et al* [45] and Fournier-Lupien *et al* [70] identify the Si–Sn as the shoulder of the Si–Ge peak (∼380 cm^{-1}), and also observe a double Si-Si peak (∼450 cm^{-1}), in samples with Si up to 19 at.%.

Features related to Sn and Si are studied with more details in ternary alloys with low Ge content. Schlipf *et al* [68] study MBE-grown samples with 5%, 7.5%, 10%, and 12.5% Sn and 8%, 27.5%, 37%, and 46% Si. Strong, asymmetric peaks were observed for both Si–Si (460 cm^{-1}) and Si–Ge (380 cm^{-1}) vibration, the latter with a possible shoulder due to Si–Sn.

Most of these studies investigated the shift of the various features as a function of the content and the strain, typically following a linear trend. The exact measurements of these linear correlations are needed for the use of Raman spectroscopy for material metrology, as discussed in section 5.

In any case, the quantitative estimation of the mode features requires the deconvolution of the spectra via peak fitting. The most critical region here is the vicinity of the Ge–Ge peak, consisting of three components: (1) the main Ge–Ge peak, (2) the DA shoulder, in principle with two separate components, (3) the Ge–Sn peak (figure 4(b)).

The proper lineshape for the first-order peak should take into account the activation of the phonon density of states

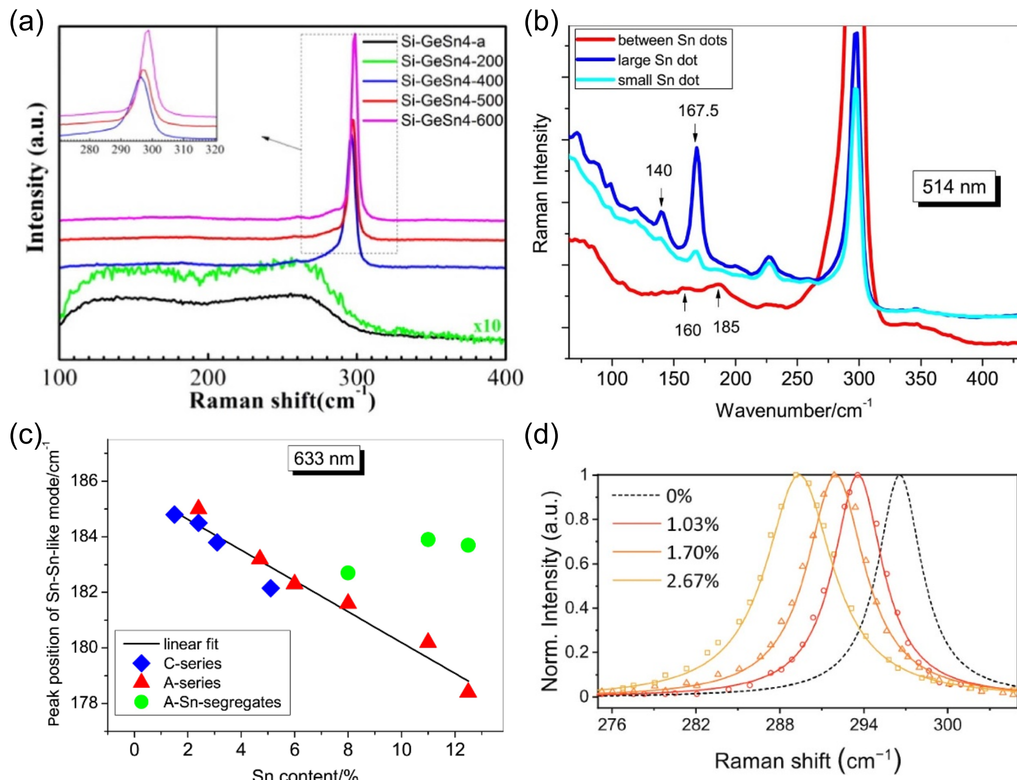

Figure 5. (a) Raman spectra of an amorphous sample with nominal 20% Sn before and after rapid thermal annealing at 200, 400, 500, and 600 °C. (a) Reprinted from [74], Copyright (2016), with permission from Elsevier. (b) Raman spectra from different locations on a GeSn sample with 12.5% Sn that presents clusters on its surface. (c) Sn–Sn peak position vs Sn content for different samples. Panel b,c (b), (c) [62] John Wiley & Sons. Copyright © 2017 WILEY-VCH Verlag GmbH & Co. KGaA, Weinheim. (d) Raman spectra from GeSn nanowires (length 5 µm and width 120 nm) with increasing tensile strain. The dashed line is from relaxed GeSn. (d) Reprinted from [75], with the permission of AIP Publishing.

and thus the optical phonon branch dispersion; this approach is usually used in studies of amorphous and nanocrystalline samples, where the disorder, confinement, and surface effects dominate [71, 72]. The large width of the spectral features, the noise level, and the limited spectral resolution do not allow a fine selection against various possible models for the peak. Therefore, in the case of these high-crystalline quality alloys, these complex models are replaced by an empirical lineshape, in particular the exponentially modified Gaussian (EMG) [60]. More specifically, the Ge–Ge peak is fitted with an EMG, while the Ge–Sn is a simple Gaussian. The DA is assumed to be a single component with a Gaussian lineshape. Alternative to the Gaussian, Voigt [73] and Lorentzian lineshape are employed, with asymmetric broadening if needed [68]. Examples of peak tagging and deconvolution can be found in ref [8, 27, 42, 61].

Finally, an important parameter enabling the observation of all the spectral features is the excitation wavelength. Fournier-Lupien *et al* [70] compare the spectra of SiGeSn with 532 nm, 633 nm, and 785 nm excitation (figure 4(c)). The 633 nm laser gives clearer spectra at all the investigated compositions, likely as a result of the quasi-resonant electron excitation at the E_1 critical point.

The excitation wavelength also defines the range of depth from the surface contributing to the measured spectra (see section 2.2). In the case of thin epitaxial layers of a few tens of nm measured with red or infrared lasers, which have a range up to 100 nm, the Raman signal from the substrate is measured together with that of the top layer, and should be considered for proper analysis [68, 70].

3.2. Amorphous layers, segregated Sn, and nanocrystals

High crystalline-quality epitaxial layers are the basis of the technological applications of SiGeSn. However, insight into the role of disorder and crystallization dynamics can be obtained in (Si)GeSn produced in amorphous form by methods such as sputtering.

For example, Zhang *et al* [74] investigate GeSn films with up to 20% Sn deposited by magnetron sputtering and studied the effect of annealing on the crystallization (figure 5(a)). In the as-deposited state, broad Raman peaks near 266 cm^{-1} (Ge–Ge) and ∼150 cm^{-1} (Sn–Sn) were observed. The integrated peak intensity correlated with Sn content. Upon annealing, the Ge–Ge peak narrows and increases in intensity, indicating crystallization. Additionally, Sn segregation was

observed, forming ∼1 μm clusters that grew with increasing annealing temperature.

Perova *et al* [62] further study these segregated Sn clusters via polarized Raman spectroscopy on GeSn samples with 8%–12% Sn grown by MBE (figures 5(b) and (c)). In these samples, the Sn–Sn peak deviated from the linear trend seen in non-segregated alloys. Instead, distinct peaks were observed near 170 cm^{-1} and 126 cm^{-1}, with the latter assigned to metallic β-Sn, and the former possibly related to Sn oxides.

Nanostructured SiGeSn systems, such as nanowires (NWs), have also been explored. Burt *et al* [75] observe symmetric peaks around 300 cm^{-1} that shift with Sn content, in tensile-strained GeSn NW fabricated by top–down methods up to 6% Sn (figure 5(d)). In a dual NW (GeSn@Ge), the signal from Ge and from GeSn can be separated in Raman spectra, enabling strain evaluation and comparison with mechanical simulations [76].

Raha *et al* [77] have studied NWs produced by liquid-injection CVD. Their Raman spectrum (at >6% Sn) has a broad, asymmetric band around 300 cm^{-1}, which is analyzed with three components, associated, with the help of atomistic simulations, with a primary Ge–Ge vibration, a 'compressed Ge–Ge' due to the presence of Sn clusters at higher energy, and a 'relaxed Ge–Ge' at lower energy. Polarized Raman spectroscopy reveals a different angular dependence of these modes, suggesting that the NW confinement and lattice deformation removed the degeneracy of the T_{2g} symmetry.

4. Polarized Raman spectroscopy and alloy ordering

The typical feature of an alloy is its disordered arrangement of atoms. The simplest model for a crystalline alloy assumes random substitutional placement of the atoms in the crystal structure (random alloy). The probability of an atom site being occupied by one of the species depends solely on the composition. The bond lengths are a linear interpolation of the lengths of the components and are the same for the Ge–Ge, Ge–Sn, Si–Ge, Si–Sn, and Sn–Sn couples in that each atom has the same random environment (virtual crystal approximation) [78, 79]. However, due to different physical constraints—e.g. bond strength, atomic size, and electronic interactions among atoms in an alloy- non-random atom distributions with specific local atomic arrangements can be energetically more favorable, realizing the so-called short-range ordering (SRO). In systems with SRO, the order is restricted to a small spatial region, typically involving nearest- or next-nearest-neighbor atoms, without extending throughout the material. Short-range ordering refers to a localized atomic arrangement dictated by immediate energetic preferences, lacking the periodicity and uniformity characteristic of long-range ordering [80].

The introduction of Sn in alloys with Si and Ge may have a significant effect on the alloy crystal and atomic structure. The higher atomic mass and larger lattice of Sn result in an extremely low solid solubility, and the epitaxial growth of (Si)GeSn is considerably challenging, occurring in conditions far from thermodynamic equilibrium [6]. In these metastable materials, the alloy configuration can deviate from the classical random alloy assumption, as it has been shown in the theoretical studies [31–33, 37, 81]. In 2020, *ab-initio* Monte Carlo simulations by Cao *et al* [31] provide the first strong suggestion that GeSn can inherently exhibits short-range order across its entire composition range. Their statistical sampling of atomic configurations show that Sn atoms are not distributed purely randomly; instead, there is a pronounced tendency for Sn atoms to avoid occupying nearest-neighbor sites with each other, realizing the so-called Sn–Sn repulsion. Jin *et al* [33] extend these ideas to medium-entropy Si–Ge–Sn alloys, finding that two distinct types of SRO can even coexist in the ternary system under certain conditions. More recently, large-scale atomistic simulations with machine-learning potentials [32] have also revealed nano-domains of SRO in GeSn, further emphasizing that SRO is an intrinsic feature of the alloy atomic structure.

Thus, detecting and understanding alloy ordering is essential because it significantly influences the structural, electronic, and optoelectronic properties. The significance of SRO lies in how local atomic arrangements influence macroscopic behaviors. The SRO affects the electronic structure by altering the local potential landscape and consequently influences the electronic states near the band edges, effectively modifying the bandgap. Simulations show that in GeSn and SiGeSn alloys, the direct bandgap increases when SRO is considered, compared to the smaller or even negative bandgap that could be predicted in the absence of SRO. The change occurs because SRO typically leads to a more stable, lower-energy state, which can increase the bandgap [33, 37].

The energy landscape defining the stability of these alloys depends on several driving forces, leading to SRO: the size mismatch induces local strain fields, direct chemical affinities or aversions between specific element pairs (for instance, Sn–Sn bonds may be energetically unfavorable), and overall thermodynamic considerations. Enthalpy and entropy balance can make certain local arrangements more stable than a random distribution [31, 37]. Kinetic factors during growth (temperature, deposition rate) also play a role, as they can freeze in metastable arrangements or allow atomic rearrangement toward particular configurations. Thus, a combination of atomic size difference, bond chemistry, and growth conditions governs the extent of SRO in SiGeSn and related alloys [82].

Experimentally, direct observation of SRO is challenging, and typical methods for accessing SRO are not of immediate use. Nonetheless, emerging techniques have started to confirm the theoretical predictions. One powerful method is atom probe tomography (APT), which can map out the 3D positions of individual atoms in a small volume. By applying statistical analysis to APT data, it is possible to detect deviations from alloy randomness. Liu *et al* [36] demonstrate a k-nearest-neighbors analysis of APT data for $Ge_{0.86}Sn_{0.14}$ that quantified SRO in real space. They show that the probability of Sn–Sn nearest neighbors fluctuates by ±15% compared

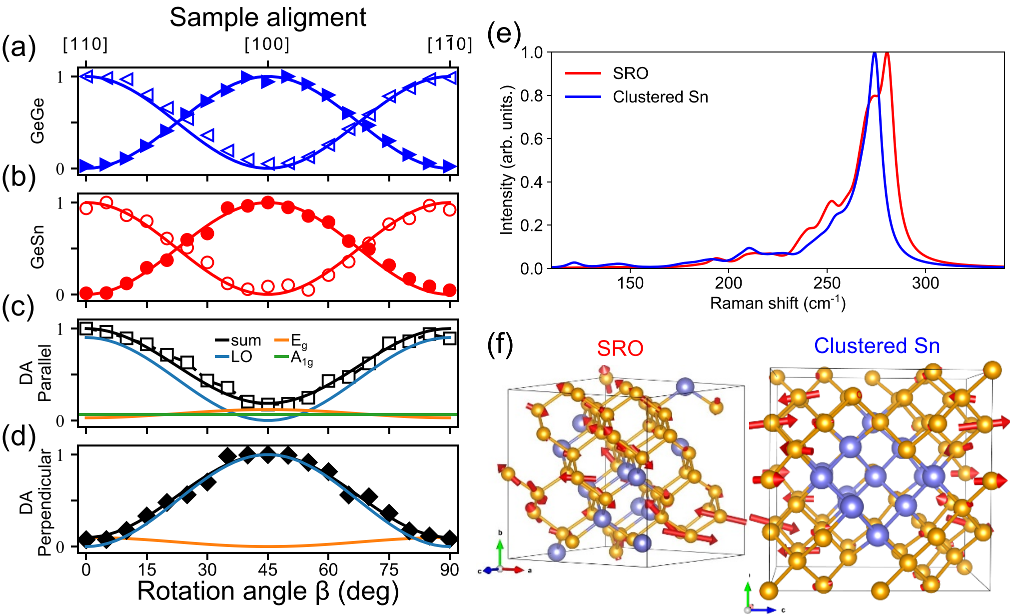

Figure 6. Angular dependence of the normalized intensity and position of the different peaks in a sample with 14 at.% Sn. Panels (a) and (b) show the intensity of the Ge–Ge and Ge–Sn vibration modes in parallel (empty symbols) and perpendicular (full symbols) polarizer alignment. The lines represent the fitting with an LO angular dependence. Panels (c) and (d) show the fitting of the angular dependence of the DA intensity with a combination of different representations. (e) DFT-calculated Raman spectra for samples with 19 at % Sn in two different ordering configurations. (f) Simulated displacement vectors obtained for the case of SRO and clustered Sn. These simulations provide insights into the vibrational modes and their contributions to the Raman spectra in GeSn alloys under different structural arrangements. (a)–(f) Adapted from [75], with the permission of AIP Publishing.

to a random alloy, confirming that some regions have an under-representation of Sn–Sn pairs while others might have slight over-representations. Interestingly, they find that Sn–Sn pairing was less favored in strained regions or when the layer was fully relaxed, but slightly more common near the surface of the film. This aligns with the notion that strain and surface effects can modulate local ordering.

Another local probe, extended x-ray absorption fine structure (EXAFS), provides complementary evidence. EXAFS measures the distribution of nearest-neighbor distances and coordination environment around a selected element by analyzing oscillations in x-ray absorption above an absorption edge. Gougam *et al* [83] employ Sn K-edge EXAFS on GeSn layers (with up to 13% Sn) and find a clear signature of SRO. The first coordination shell around Sn is dominated by Ge atoms, strongly suppressing Sn–Sn bonds, whereas in the second-neighbor shell, the presence of Sn–Sn is enhanced relative to random.

While techniques like APT and EXAFS can directly reveal SRO, they have limitations. APT is destructive, requires sophisticated instrumentation, and samples only tiny volumes. EXAFS needs synchrotron radiation and provides ensemble-averaged local structure information. Neither can be easily performed as a routine characterization. This has motivated the search for more accessible, lab-based methods to sense local ordering. One promising approach that has emerged is polarization-resolved Raman spectroscopy [42, 61]. It can provide a powerful method to probe local lattice distortions, bond-specific interactions, and consequently SRO. Unlike conventional Raman measurements, the polarization configuration allows the separation of vibrational modes according to their symmetry , as described in section 2. Specifically, in perfectly ordered crystals, only definite phonon modes are Raman-active due to strict selection rules. In real alloys, however, deviations from ideal symmetry due to compositional fluctuations, lattice distortion, and disorder activate additional modes and alter their angular dependence. Investigating energy shifts and relative intensity variations under different polarization conditions made it possible to associate Raman modes with atomic pair vibrations and lattice short-range order. The spectra provide information, particularly regarding the peaks associated with second-order scattering (overtones and combinations), which are also present in unalloyed materials. This method is particularly effective when coupled with numerical simulations of vibrational modes under various disorder configurations. DFT simulations provide insight into the movement of atoms in an alloy supercell, directing the interpretation of experimental Raman spectra.

With the use of angular-resolved polarized spectroscopy, the modes associated with pair vibrations, even in a strained lattice, belong only to $T_{2g}(LO)$ representation, and thus will be observed in 'allowed' configurations (see section 2). Instead, the disorder-associated features are expected to be found in all the configurations. Thus, when the A_{1g} and E_g representations give non-zero signal but the T_{2g} is suppressed ('forbidden' configurations), the spectral features can be assigned to disorder or to high-order scattering.

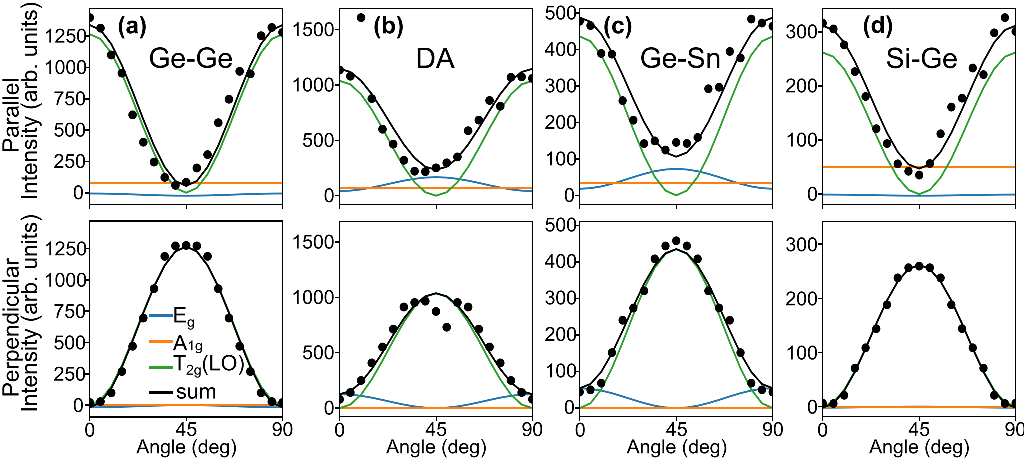

Figure 7. Angular dependence of (a) Ge–Ge, (b) DA, (c) Ge–Sn, (d) Si–Ge, (e) Si–Si peaks of SiGeSn. Reprinted with permission from [42], Copyright (2024) by the American Physical Society. The data are analyzed as a sum of components belonging to representations A1g, Eg, and T2g (only LO component).

In Corley-Wiciak *et al* [61], the angular dependence of the intensity and energy of the modes in GeSn is investigated (figure 6(a)), using the patterns reported in table 2. While the Ge–Ge and Ge–Sn were confirmed to be LO modes, with intensity reaching zero at specific rotation angle with a quadrupolar pattern (figure 2(b)), the DA was instead found to be a mixture of (at least) two modes, observed as a non-zero intensity in the parallel alignment at rotation of 45°. In fact, the energy of the DA is also found to be dependent on the rotation angle, suggesting the presence of two non-resolved modes, one following the LO angular pattern and one 'non-LO', with different energy. The comparison with DFT calculations allows to associate these spectral features with local arrangements of the alloy.

The Ge–Ge and DA(LO) modes are both due to Ge–Ge pairs, the latter being affected by a distorted local environment, and the former associated with pairs whose bonds are least affected by local environmental distortion (figures 6(b) and (c)).

As a function of Sn content, the DA(LO) intensity increases faster than disorder-related DA($A_{1g}+E_g$) components, highlighting the stronger impact of the distorted environment on the spectrum. In particular, the DA(LO) mode becomes more prominent at higher Sn content, consistent with DFT calculations, suggesting the onset of short-range order above 10% Sn. Ge–Sn mode appears less sensitive to further Sn addition.

In ternary SiGeSn [42], a similar analysis also revealed that vibrational dynamics involves a complex interplay of modes, with the DA peak being particularly sensitive to local arrangements. An angular study of the intensities of DA, Ge–Sn, Ge–Ge, Si–Ge, and Si–Si peaks (shown in figure 7) highlighted the mixed nature of these components linked to lattice deformation. This separation of different symmetries deepened the understanding of how the alloy vibrational dynamics respond to changing composition, revealing the complex interplay of elements. Higher intensities of Ge–Sn and Si–Ge vibrations and a simultaneous decrease in Ge–Ge vibration intensities suggest that Sn atoms tend to repel other Sn and Si atoms.

5. Measuring the lattice strain and composition

The accurate measurement of strain and composition in GeSn and SiGeSn semiconductor alloys is essential, as these parameters directly influence the electronic band structure and optical properties of the material. As anticipated in the introduction, the incorporation of different amounts of Sn (and Si) in the alloy can be used to modify the electronic band structures, and consequently the carrier effective masses and mobilities. The same can be attained by acting on lattice strain, i.e. by intentionally inducing a compressive or tensile strain to the cubic lattice cells of the alloys. As an example, an in-plane tensile lattice strain decreases the fundamental band gap and promotes its 'directness', while vice–versa a compressive strain is detrimental in achieving a direct band gap material [21, 84, 85]. Consequently, strain engineering, either acting on external stressor or leveraging on the heteroepitaxial strain, can be used to tailor the optoelectronic properties of a (Si)GeSn alloy of a given composition. Raman spectroscopy is highly suitable in characterizing simultaneously strain and composition in SiGeSn alloys. Indeed, it provides a rapid, nondestructive method to assess both strain and composition in GeSn and SiGeSn alloys, based on the shifts in the lattice vibrational frequencies. By analyzing the energy position, width, and intensity of phonon modes, that information can be extracted with a sub-μm spatial resolution. Peak fitting, often using Voigt, Lorentzian, or EMG profiles, allows precise determination of phonon frequencies with sub-wavenumber precision. Moreover, selecting the laser excitation wavelength provides the opportunity to probe the material at different

penetration depths and observe resonance enhancements (see section 3).

Incorporating heavier Sn atoms into the Ge lattice matrix (or SiGe) shifts the main Raman modes to lower energy because of the larger mass of Sn and lattice perturbation that reduces the bond vibrational frequency. These trends are observed consistently in the Ge–Ge, Ge–Sn, DA, and Sn–Sn peaks, although the magnitude of the shift varies between different modes. Interestingly, the Sn content impact on the Raman modes change depending on the polarization configurations, since modes of different symmetry respond differently to the composition variation [42]. Besides composition, strain affects the phonon energy as well. Tensile strain, which elongates bonds and expands the lattice, lowers the optical phonon frequency (redshift), while compressive strain does the opposite (blueshift). Because both composition and strain of alloys shift the Raman peak positions, a critical task is to decouple these two effects. Typically, linear models for the shift of the peak position and the composition and strain are employed.

In the case of binary GeSn alloys, the Ge–Ge mode is considered, and the two relevant material parameters are Sn concentration (x) and in-plane strain ($\varepsilon_{||}$) [45]:

$$\omega_{\mathrm{Ge-Ge}} = \omega_{0,\mathrm{Ge-Ge}} + a \cdot x + b \cdot \varepsilon_{||}. \quad (5)$$

Here, $\omega_{0,\mathrm{Ge-Ge}}$ is the unstrained phonon frequency for pure Ge, a is the compositional (Sn-induced) shift coefficient, and b is the strain-induced shift coefficient.

For ternary SiGeSn alloys, where additional substitutional elements introduce further modifications to the lattice dynamics, a similar but more complex relationship is employed [45]:

$$\omega_{\mathrm{Ge-Ge}} = \omega_{0,\mathrm{Ge-Ge}} + a_{\mathrm{Sn,Ge-Ge}} \cdot x_{\mathrm{Sn}} + a_{\mathrm{Si,Ge-Ge}} \cdot x_{\mathrm{Si}} + b_{\mathrm{Ge-Ge}} \cdot \varepsilon_{||}. \quad (6)$$

In this case, both the Sn and Si contents contribute to the phonon shift, each with its own compositional coefficient. Analogous formulations can also be applied to other vibrational modes within the alloy system:

$$\omega_{\mathrm{Si-Ge}} = \omega_{0,\mathrm{Si-Ge}} + a_{\mathrm{Si,Si-Ge}} \cdot x_{\mathrm{Si}} + b_{\mathrm{Si-Ge}} \cdot \varepsilon_{||} \quad (7)$$

$$\omega_{\mathrm{Si-Si}} = \omega_{0,\mathrm{Si-Si}} + a_{\mathrm{Sn,Si-Si}} \cdot x_{\mathrm{Sn}} + a_{\mathrm{Ge,Si-Si}} \cdot (1 - x_{\mathrm{Si}} - x_{\mathrm{Sn}}) + b_{\mathrm{Si-Si}} \cdot \varepsilon_{||}. \quad (8)$$

Accurate calibration of each coefficient is essential to distinguish the overlapping effects of alloying and strain. Numerous experimental studies [8, 57, 60–62, 67, 68, 70, 86–94] have provided a wide range of coefficient values depending on factors such as sample strain state, content range, and measurement conditions. Comparing reported coefficients across different investigations helps identify consistent trends and refine the parameter space used for quantitative analysis. Figure 8 and table 3 show a collection of a and b coefficient values reported in literature for the Ge–Ge mode in GeSn alloys under various strain conditions and for different Sn contents. The compositional shift coefficient a varies within the [−68; −95] cm^{-1} interval, with outliers at −33.8 cm^{-1} and −140.6 cm^{-1}; the slightly higher values are typically observed for relaxed layers. The strain shift coefficient b exhibits a larger variation, from ∼−284 cm^{-1} to over −560 cm^{-1}, with outliers at −76.8 cm^{-1} and −64 cm^{-1}, depending on the methodology and strain calibration approach.

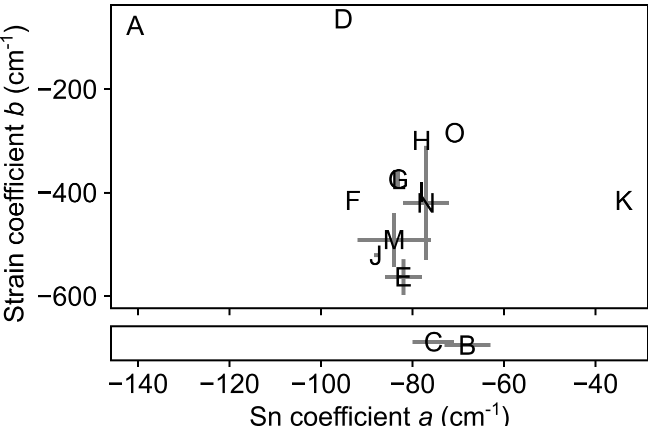

Figure 8. Distribution of the Sn- and strain-shift coefficient values from literature for the Ge–Ge peak in GeSn alloys. Letters refer to table 3. The bottom box reports the cases for which only the Sn-shift coefficient a is available. Error bars are as reported in the references (see table 3).

Table 4 presents the composition and shift coefficients a and b relative to the other Raman modes (Ge–Sn, DA, Sn–Sn), which are particularly useful for validating Raman fitting models. The Ge–Sn peak generally shows a compositional shift coefficient a in the [−38; −68] cm^{-1} range with associated strain coefficients ranging from −160 to −347 cm^{-1}. The DA mode presents a value in the [−29; −53] cm^{-1} range. For the Sn-Sn peak, a strong compositional dependence is observed, with a ranging from −78 to −106 cm^{-1}.

The variance among the values is associated with experimental errors in determining the strain or composition, in the exact determination of the peak position (especially for low-intensity secondary modes), but also on the use of different data analysis approach [86] or a not-resolved interplay between strain and shift [62]. For the main Ge–Ge peak, as shown in figure 8, the values obtained in more recent papers with the standard definitions reported above are dense around a∼−80 cm^{-1} and b∼−450 cm^{-1}, in the range for Sn $<$ 20 at.%.

Table 5 focuses on ternary SiGeSn alloys, where both Sn and Si influence the phonon structure. The ability to extract individual compositional coefficients in such alloys depends heavily on high-quality fitting of multiple Raman modes. Reported values show agreement between studies.

When multiple Raman peaks can be measured (e.g. Ge–Ge and Ge–Sn), it is possible to extract both composition

Table 3. Coefficients for composition and strain shift the main Ge–Ge mode in GeSn. Values are at room temperature.

	References	ω_0 cm^{-1}	Sn-shift *a* cm^{-1}	Strain-shift *b* cm^{-1}	Laser excitation nm	Sn %	Strain	Substrate
A	Rojas-López *et al* [86]		−140.6	−76.8	514	0–22	Fully strained	Ge
B	Li *et al* [87]		−68 ± 5		514, 633	0–20	relaxed	Ge
C	D'Costa *et al* [60]		−75.4 ± 4.5		514	0–18	0.004%	Si
D	Su *et al* [88]		−95.1	−64	532	0–8	Relaxed, fully strained	Ge or Si
E	Lin *et al* [89]		−82 ± 4	−563 ± 34		4–8		InGaAs
F	Fournier-Lupien *et al* [70]		−93	−415	633	2–12	Relaxed, up to −1.56%	Ge
G	Cheng *et al* [90]		−83.11 ± 0.01	−374 ± 15.60	532	0–8	Relaxed, strained	Ge
H	Chang *et al* [92]		−78	−299.3	488	0–8.3	−0.5% to −1.5%	Ge
I	Takeuchi *et al* [57]		−78	−399	532	0–3	0 to −0.5%	Ge
J	Gassenq *et al* [86]		−88	−521	532	6–15	Relaxed and fully strained	Ge
K	Perova *et al* [62]		−33.8 ± 0.4	−415	633	0–8	0.2%	Ge
L	Vasin *et al* [94]		−83	−375	633	0–4	Relaxed	Ge
M	Bouthillier *et al* [8]	300.4 ± 0.9	−84 ± 8	−491 ± 52	633	5–17	Relaxed and pseudomorphic	Ge
N	Corley-Wiciak *et al* [61]	301.0 ± 0.3	−77 ± 5	−420 ± 110	633	5–15	Relaxed	Ge
O	Zhao *et al* [67]		−70.77	−284.35	532, 633, 785	2–31	Relaxed and strained	GeGaAs

Table 4. Coefficients for composition and strain shift for Ge–Sn, DA and Sn–Sn peaks in GeSn.

Mode	Ge–Sn			DA			Sn–Sn		
	ω_0	*a*	b	ω_0	*a*	b	ω_0	a	b
References	cm^{-1}	cm^{-1}	cm^{-1}	cm^{-1}	cm^{-1}	cm^{-1}	cm^{-1}	cm^{-1}	cm^{-1}
Perova *et al* [62]	263 ± 0.5	−38.3 ± 5.1		287.2 ± 0.5	−29.4 ± 3.7			−78.7	−189.7
Bouthillier *et al* [8]	261 ± 1	−68 ± 11	−347 ± 69	291.3 ± 0.7	−49 ± 7	−347 ± 45	188 ± 1	−104 ± 9	−292 ± 59
Corley-Wiciak *et al* [61]	262.8 ± 0.4	−52 ± 7	−160 ± 140	294 ± 1	−53 ± 20	−40 ± 400	189 ± 1	−83 ± 10	−140 ± 90
Zhao *et al* [67]		−49.73	−226.87					−106.86	−203.2

Table 5. Coefficients for composition and strain shift in SiGeSn as in equations (6)–(8).

References	$a_{Sn,Ge–Ge}$ cm^{-1}	$a_{Si,Ge–Ge}$ cm^{-1}	$b_{Ge–Ge}$ cm^{-1}	$a_{Si,Si–Ge}$ cm^{-1}	$b_{Si–Ge}$ cm^{-1}	$a_{Ge,Si–Si}$ cm^{-1}	$a_{Si,Si–Si}$ cm^{-1}	$b_{Si–Si}$ cm^{-1}
D'Costa *et al* [60]	−94.0 ± 7.1	−17.1 ± 2.6	−415	−110	−575	−71.2 ± 1.7	−213 ± 12	−984
Fournier-Lupien *et al* [70]	−93.5	−19.2	−415	−166	−575	−80	−160	−984
Schlipf *et al* [68]	−89. ± 2.9	−19.4	−402 ± 49	−145.6 ± 3.0	−389 ± 51	−82.9 ± 0.5	−107.7 ± 4.7	−607 ± 96

and strain directly from the Raman measurements, solving a system of equations incuding the shift coefficients [48]. However, in many cases, only the Ge–Ge mode is strong enough to be reliably fitted. In such cases, one parameter (usually composition) must be assumed based on external data from complementary techniques, and Raman is used to extract the strain. To improve accuracy and cross-validation, Raman spectroscopy is often combined, for example, with x-ray Diffraction (XRD) to measure average strain or composition, Rutherford backscattering (RBS), and secondary ion mass spectrometry, for compositional profiling.

As an example, figure 9 shows three spectra from epitaxial GeSn/Ge samples with ∼12 at.% Sn verified by RBS [27, 61]. The spectra present the main features around 300 cm^{-1}. The samples have different thickness resulting in different

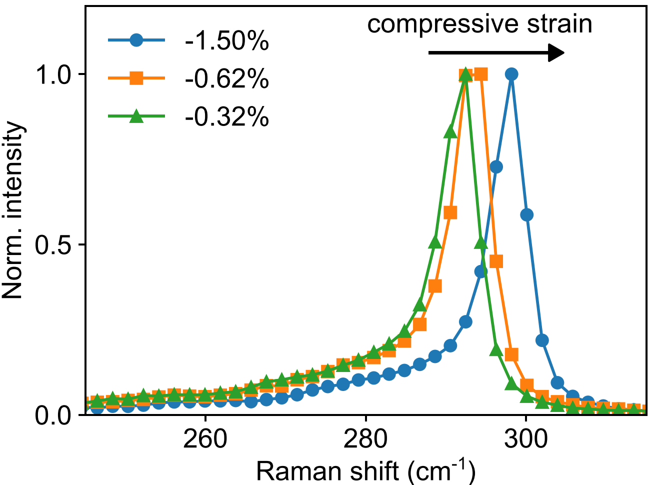

Figure 9. Raman spectra a set of samples of GeSn at ~12 at.% Sn content, with thickness of 90, 290, 700 nm and strain −1.50%, −0.62%, −0.32%, respectively. Spectra are acquired using 532 nm excitation at room temperature.

compressive biaxial strain, as verified by XRD [27]. As the layer is more compressively strained ($\varepsilon_{\|}$ from −0.32% to −1.50%), the peak shifts to higher Raman shift.

6. Mapping and application to devices

Raman imaging is employed in microelectronics as a diagnostic tool, together with the metrology described in section 5 [95–97]. In this way, analysis of the composition and strain of devices and other microstructures can be readily obtained. One key application is strain mapping, that is especially interesting when the device is subject to mechanical forces that induce a strain distribution over its volume, for example in the case of micro-electromechanical systems [98], or when 3D microstructures are fabricated for lasing, such as the microdisk geometry (figure 10(a)) [7, 93, 99, 100]. As an example, we show in figure 10 the peak position and strain measured on a microdisk. These maps are acquired with nominal step size of 0.3 μm and a spot size of ~0.5 μm, so that the spectrum at each pixel is the convolution of those in the nearby region. Nevertheless, the trend of the peak shift is clearly observable, enabling the identification of the strain distribution along microstructure. The strain is then calculated with the formula reported in section 5, knowing the composition of the disk. The strain mapping in GeSn exhibits a robust correlation with structural characterization based on x-ray diffraction for microdisks [101], which have emerged as a model system for mid-infrared group-IV lasers.

The relationship between Raman and strained microstructure is indeed two-way: on one side, there is the interest in measuring the strain by optical methods; thus, the spectroscopy is a diagnostic tool for verification of process results and for comparison with optical experiments. On the other hand, the calibration of the strain-shift coefficient can be obtained by measuring the spatial dependence of the spectra in a structure with a known strain distribution, derived from micromechanical fabrication. This enables the estimation of the phonon-deformation potentials p,q,r, that are proportional to the curvature (Hessian) of the interatomic potential [54].

In details, the energy ω_k of the three-fold degenerate phonon modes of the O_h group splits under a general deformation ε_{ij}, and is given by first-order perturbation theory as the eigenvalues of the matrix [103]

$$\Psi(\varepsilon) = \begin{pmatrix} p\varepsilon_{xx} + q(\varepsilon_{yy} + \varepsilon_{yy}) & 2r\varepsilon_{xy} & 2r\varepsilon_{xz} \\ 2r\varepsilon_{xy} & q\varepsilon_{xx} + p(\varepsilon_{yy} + \varepsilon_{yy}) & 2r\varepsilon_{yz} \\ 2r\varepsilon_{xz} & 2r\varepsilon_{yz} & p\varepsilon_{zz} + q(\varepsilon_{xx} + \varepsilon_{yy}) \end{pmatrix}. \quad (9)$$

The eigenvalues are given by

$$\lambda_k = \omega_k^2 - \omega_0^2 \cong 2\omega_0(\omega_k - \omega_0) \quad (10)$$

where $\omega_k = \omega + \Delta\omega$ and $\Delta\omega \ll \omega_0$ In case of uniaxial or biaxial strain ($\varepsilon_{ij} = 0$ for $i \neq j$), the matrix is diagonal, and the eigenvalues are immediately found in terms of p and q. Selections rules related to the structure of the experimental setup for a complete picture of the strain characterization and related deformation potentials can be observed in [104].

This analysis must be coupled to the study of the mechanical deformation. Here, to fully capture the phonon deformation potentials, a key role is played by numerical (finite-element) methods, which can predict the strain in structures of various geometries, given the material properties and mechanical forces, and boundary conditions.

For example, the measurement of Raman on GeSn membranes in [98] allows fundamental depth studies, both experimentally and theoretically. The relationship between Raman shift and strain for uniaxially stressed GeSn along $\langle 100\rangle$ and $\langle 110\rangle$ directions is investigated. Moreover, the compositional dependence of phonon-deformation potentials is analyzed, showing that q decreases with Sn composition, while p exhibits a more complex dependence.

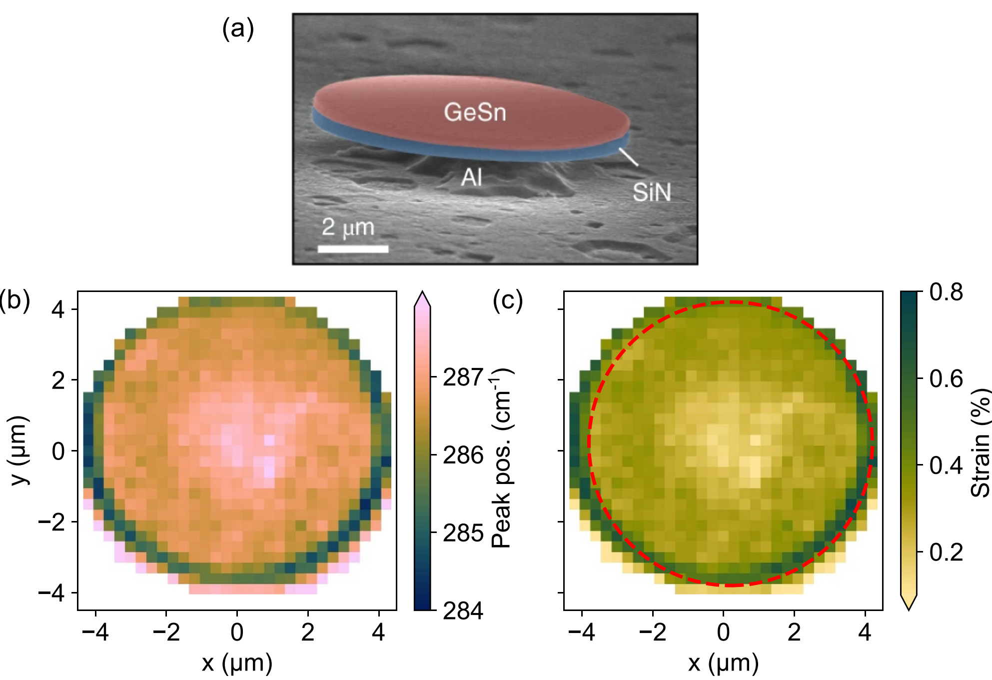

Figure 10. (a) Example electron microscope image of a microdisk. (a) Reproduced from [7], with permission from Springer Nature. (b) Peak position and (c) calculated strain in a microdisk (8 μm diameter) of GeSn wrapped into a SiN stressor layer. Data derived from [102]. Dashed line marks the disk edge.

In the case of microdisk geometry, two pioneering studies on GeSn devices [93, 100] show the significance of calibrating Sn-induced strain shift through Raman spectroscopy. Additionally, they also reveal that strain stability under optical pumping conditions can be tailored through geometry, Sn concentration, and substrate selection.

For application in lasers, the suspended microdisk geometry is often employed, comprising a central pedestal supporting a microdisk of the active material. This geometry is particularly advantageous for fabrication by a combination of isotropic and anisotropic etching, and yields strain relaxation. In relaxed layers, the minimum of conduction band decreases in energy, realizing a system with a direct band gap or close to it. Additionally, the fabrication of suspended GeSn microdisks introduces strain gradients across the device. These gradients play a crucial role in carrier localization, mode confinement, and optical gain enhancement [7, 100, 102, 105, 106].

For example, in [99], a novel dual-insulator GeSn-on-insulator (GeSnOI) material platform is used to produce strain-relaxed GeSn microdisks directly on the substrate. By undercutting only one insulating layer (Al_2O_3), the microdisks are supported by SiO_2. The removal of undesirable compressive strain is confirmed by Raman maps. Additionally, this method can confirm excellent thermal management and optical confinement.
Elbaz

et al [107] employ spatially resolved Raman spectroscopy to map the residual strain distribution in GeSn microdisks. An interplay between strain and relaxation is observed, as the residual compressive strain remains at the center of the specimen. Concurrently, the outer edge partially relaxes, and the defect density is removed, forming a gradient that is confirmed via Raman shift profiles. The anisotropy inherent in the strain landscape gives rise to a potential well that confines carriers, thereby contributing to the reduction of the lasing threshold. It is important to note that the spatial carrier trapping leads also to a decrease of non-radiative recombination, particularly within the central cavity region where strain is more controlled and the optical mode intensity is the highest.

This study demonstrates the significance of Raman strain mapping in two distinct capacities: firstly, as a post-fabrication tool, and secondly, as a predictive design metric. The comprehension of strain accumulation or relaxation facilitates the engineering of gain regions by numerical simulations.

This approach was used in [108], where Raman strain maps are used to provide data for band structure simulations, leading to a strong level of internal agreement. Furthermore, a temperature-dependent Raman characterization is also shown, indicating that a decrease in temperature by approximately 180 K results in an additional tensile biaxial strain of approximately 0.1% in the center of the disks. It is also observed that the relaxed area of the microdisk exhibits a reduced susceptibility to thermomechanical effects, as GeSn is no longer in direct contact with the Ge and Si substrate, thereby allowing for unconstrained contraction. The authors demonstrated that the strain-induced variation in the band gap along the disk's surface exhibits a range of 30 meV (figure 11(a)). They further establish

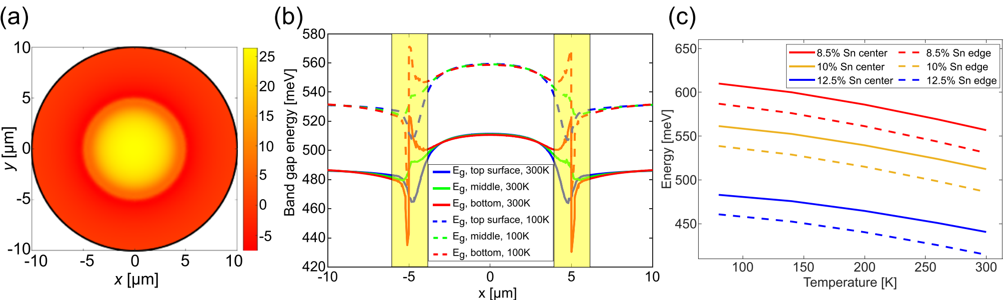

Figure 11. Bandgap simulations in a strained microdisk. (a) Color map of the energy gap extracted 2 nm below the surface; (b) energy gap profiles extracted along the horizontal line cut at room T (continuous lines) and 100 K (dashed lines) at the top (blue), middle (green) and bottom (red) of the disk. The area surrounding the pedestal is in yellow; (c) energy gap as a function of temperature for 8.5% Sn concentration (red), 10% Sn concentration (green) and 12.5% Sn concentration (blue) on the center (continuous) or the edge (dashed) of the microdisk. Reproduced with permission from [108]. CC BY-NC-ND 4.0.

that a decrease in sample temperature results in a substantial increase in the energy gap, exceeding 40 meV. Additionally, they emphasize the pivotal role of the pedestal (figure 11(b)). Furthermore, they ascertain that a variation in Sn ranging from 8.5% to 12.5% leads to a band gap variation of over 150 meV (figure 11(c)).

Also, it is important to note that without precise data on spatial strain, PL measurements could be misinterpreted, especially near heterointerfaces or patterned edges. The analysis in [108] clearly shows how measuring strain in experiments helps in understanding band structure and predicting optical performance. It emphasizes the Raman function as a link between structural and optoelectronic characterization.

Finally, while microdisks use natural strain relief from etching, it is possible to manipulate actively the strain distibution [106]. The mechanical design is approached in the following manner: long GeSn bridges are undercut from the substrate to form suspended nanostructures that accumulate uniaxial tensile strain due to built-in lattice mismatch and stress release. In this case, Raman maps reveal strain values of approximately 2%, with a localized concentration at the bridge center, exhibiting a gradient toward the edge. The GeSn/Ge membranes are utilized alongside techniques for redistributing strain fields, enabling the precise and sustained modification of the strain state within the central micro-cavity. Raman and photoluminescence spectroscopy unambiguously demonstrate the loss of strain in the cavity during arm expansion. Specifically, the device exhibits tunable lasing emission when the pump is altered. For this, it is worth saying that, through an accurate design of bridge dimensions, a strain tunability on demand, with mechanical actuators or thermal stimuli, isx demonstrated.

Similarly, Burt *et al* [99] present a geometric strain-inversion technique that uses harmful compressive strain to create beneficial tensile strain in GeSn NWs, which drastically increases the directness of the band structure. They achieve a uniaxial tensile strain of 2.67% in NWs with a width of 120 nm. More interestingly, the same lithographic approach has been used to convert the strain in GeSn by fabricating microbridges [109]. Utilizing this approach and tuning the design parameters of the microbridges, multiple lasers with different tensile strains can be achieved on a single chip.

Another example is in the domain of CMOS-compatible mid-infrared photonics. Here, Sn-graded GeSn photodetectors on Si substrate are an interesting advancement for cutoff wavelength >3 μm [110]. The graded Sn profile and strain relaxation strategy enable higher Sn incorporation while maintaining the crystalline quality that is critical for device performance. Raman spectroscopy is essential here because it enables the non-destructive mapping of strain and composition across the graded GeSn layers, providing key feedback on growth quality and structural uniformity and verifying the effectiveness of the strain-relaxation design.

7. Temperature dependence

7.1. *Effect of temperature on phonon modes and Raman spectra*

Temperature affects the intensity, energy position, and width of the Raman modes because of the anharmonic interaction of phonons. Analysis of this temperature dependence spectra provides valuable insight into phonon dynamics, also in the case of nanostructures [73, 111, 112]. From a materials characterization perspective, described in section 5, understanding the temperature dependence is crucial for disentangling the effects of strain and composition, especially in devices operating at cryogenic temperatures. Finally, the use of Raman features to measure the local temperature of samples allows for the study of heat transport in the sample.

The study of temperature dependence usually focuses on the peak position and width, rather than absolute intensity [73, 111]. In the specific case of (Si)GeSn alloys, the complex deconvolution and peak tagging suggest using the position of the dominant Ge–Ge mode.

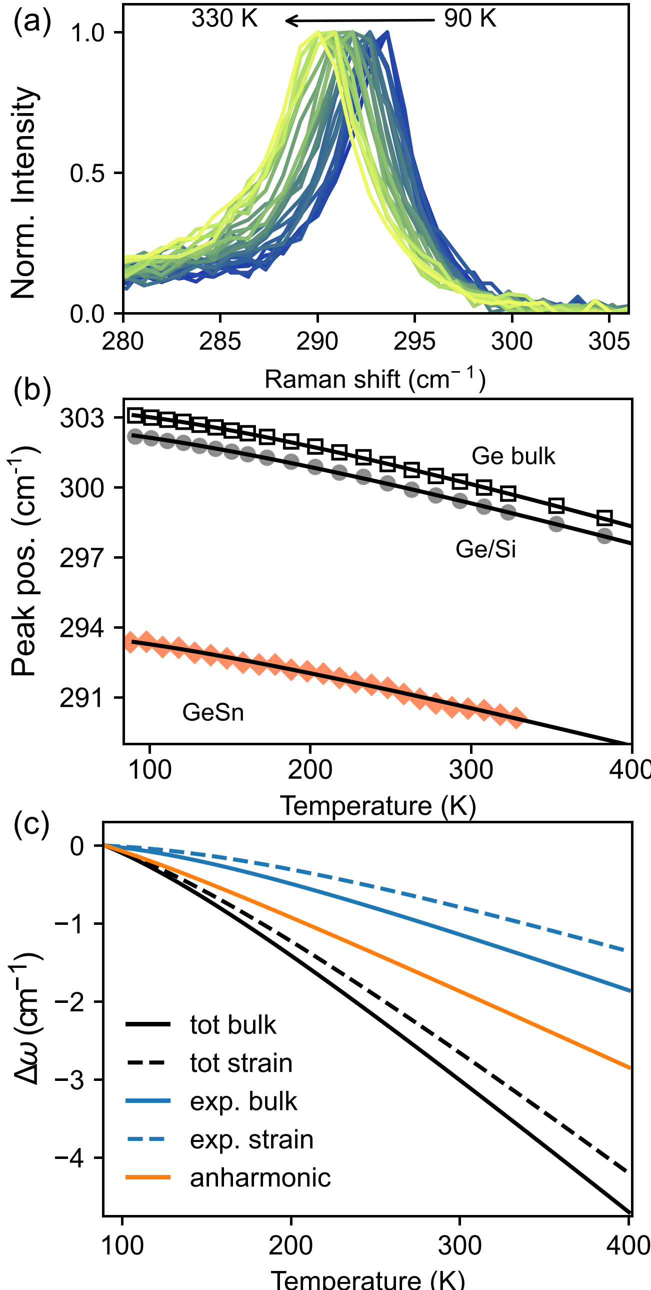

Figure 12. (a) Raman spectra of $Ge_{0.86}Sn_{0.14}$/Ge/Si at different temperatures. (b) The extracted peak position for a bulk Ge, a strained Ge layer on Si, and $Ge_{0.86}Sn_{0.14}$/Ge/Si (symbols); lines are the result of a fit comprising anisotropic thermal expansion and anharmonic interaction. (c) Calculated temperature dependence of the energy shift $\omega = \omega(T){-}\omega(90\ K)$ for bulk Ge and a strained Ge/Si layer. Reprinted with permission from [111], Copyright (2024) by the American Physical Society.

Figures 12(a) and (b) compares two cases, that of a Ge wafer, and a GeSn/Ge/Si heterostructure. While both show similar trends, in the Ge case the temperature dependence is linked to the properties of the single material, while for the heterostructure the effect of differential thermal expansion between the layers plays a role. When the sample cools down after epitaxy at high temperature, the layers contract with a different rate; the final state has the thin top GeSn layer that is deformed to remain adherent to the substrate.

In the spectrum, increasing temperature causes the peak shift to lower energy and its broadening. The energy shift occurs as an effect of high-order terms of the interatomic potential as well as the thermal lattice expansion (explicit and implicit anharmonicity [113]). The former depends on the phonon density of states and the strength of the anharmonic interaction, and is usually described with an effective model with 3- and 4-phonon interaction [114], with the 4-phonon term often assumed negligible [112]. The latter correlates the mode energy to the unit cell volume, and is controlled by the Grüneisen parameter [113, 115]. In the case of epitaxial layers, such as the (Si)GeSn thin layers, the thermal expansion of the epilayer is constrained by the substrate, yielding an anisotropic expansion (that would require a Grüneisen tensor rather than a scalar), and an unavoidable link between strain and temperature [116].

To analyze this behavior, a comprehensive model incorporating both explicit anharmonicity and constrained thermal expansion has been developed for epitaxial layers [111]. This model accurately describes the temperature dependence of Raman shifts and can be used for strain metrology. The results of this model for an heterostructure of Ge on Si are shown in figure 12(c), where the thermal expansion is compared in the case of an unstrained bulk and a strained layer, together with the explicit anharmonic term. All these terms have a comparable effect and similar trend with temperature, indicating that none of them can be ignored in modeling. By comparison with temperature-dependent XRD and Reciprocal Space Mapping, we could analyze the peak energy for Ge and GeSn epitaxial layers in the range 90–400 K and extract the relevant parameters, as reported in [111]. The result of this analysis is focused on the Ge–Ge peak showed that the Grüneisen parameters for in-plane and out-of-plane expansion is the same and compatible with the reported value for Ge bulk ($\sim$1.3); the explicit anharmonicity does not depend on alloy composition (5–14 Sn at.%), nor on the density of extended defects (dislocation defect density in the range 7×10^6–4×10^8 cm^{-2}), the strain-shift coefficient is of the order of -500 cm^{-1}, independent of composition and weakly dependent on temperature, and the composition-shift coefficient is—100 cm^{-1}, independent of temperature and strain. Though slightly less precise than other advanced techniques, this temperature-dependent Raman approach supports and complements the results presented in section 5, and allows for strain estimation across temperature ranges, as shown in figure 13(a).

Bagchi *et al* [73] investigate GeSn and SiGeSn alloys in the range 10–400 K. They find that the temperature dependence for GeSn and SiGeSn matches that of Ge. Focusing on the width and asymmetry of the peak to elucidate the scattering mechanisms and isolate the contribution of the alloy in comparison to pure Ge, the alloy contribution is found to be temperature independent. For GeSn, as a function of the Sn content (0%–12%), they found that both these parameters increase sharply for Sn content >4% (figure 13(b)), suggesting that a threshold of Sn content is required to activate the alloy scattering processes. The strength of the direct anharmonicity

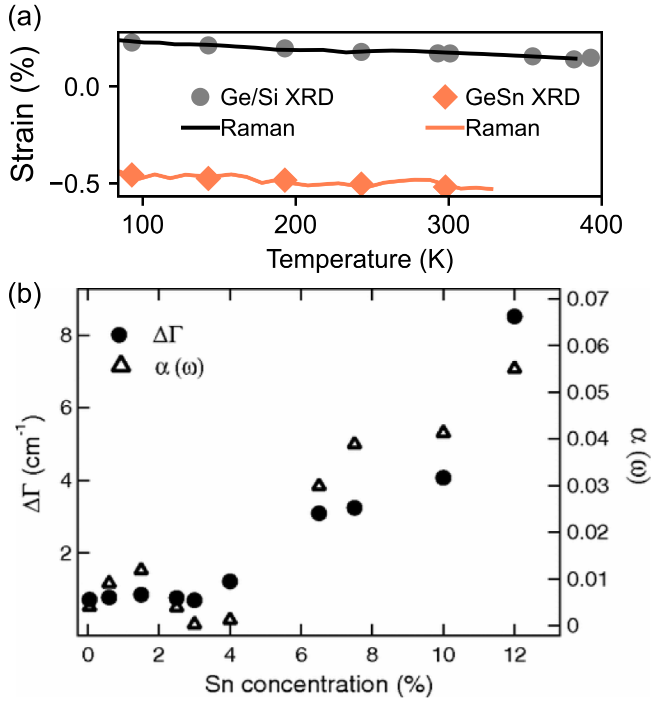

Figure 13. (a) Biaxial strain, measured by temperature-dependent XRD (symbols), and extracted from Raman data for the Ge/Si and $Ge_{0.86}Sn_{0.14}$/Ge/Si samples. Reprinted with permission from [111], Copyright (2024) by the American Physical Society. (b) Evolution of width (circles) and asymmetry (triangles) of the Ge–Ge peak with Sn content. Reprinted with permission from [73], Copyright (2011) by the American Physical Society.

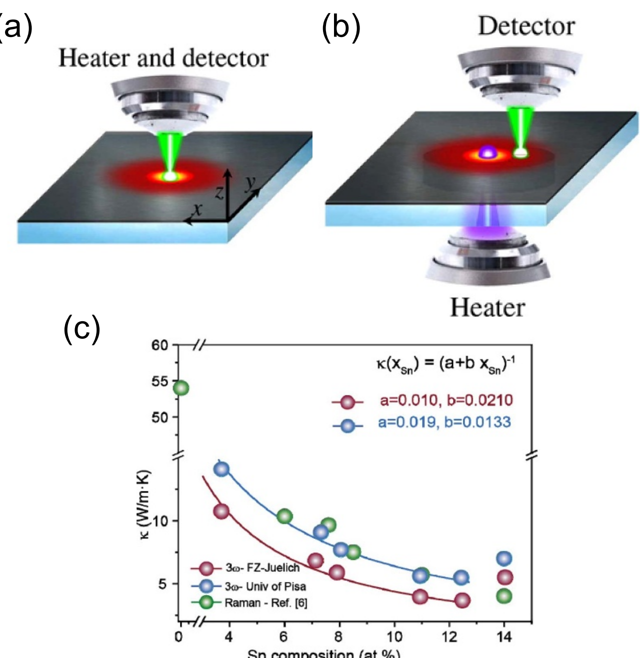

Figure 14. (a), (b) Scheme of Raman thermometry with one and two lasers. (a), (b) Reprinted from [117], with the permission of AIP Publishing. (c) Thermal conductivity at room temperature of GeSn epitaxial layers measured by Raman spectroscopy, in comparison with the 3ω method. Continuous lines are an empirical fit to the data. Reproduced from [28]. CC BY 4.0.

was found to be robust against the composition and similar to bulk Ge, while in [111] it was found to be independent of the composition for GeSn, but larger than Ge. The broadening of Raman peaks with temperature arises primarily from phonon–phonon scattering, while defect-related broadening remains constant across temperatures. The overall linewidth can thus be modeled as the sum of a temperature-independent term and a Bose–Einstein-distributed term related to phonon density of states [73].

Another feature that can be evaluated using temperature-dependent Raman spectroscopy is the thermal stability of the alloy. At elevated temperatures, Sn segregation can occur, forming β-Sn 'droplets' on the surface [30]. Liu *et al* [112] investigate GeSn up to 850 K, and found that for a sample with 8% Sn, an abrupt change is observed in the Raman spectrum at 690 K with a shift of the peak to higher energy. This result is assigned to the segregation of Sn and relaxation of the epitaxial layer. In a sample with 5% Sn, this was not observed up to 850 K, suggesting a composition-dependent segregation threshold.

7.2. *Raman thermometry*

The dependence of spectral features on temperature can be used as a thermometer to monitor the thermal effects in the sample, e.g., operating devices, or to extract the thermal conductivity of the materials [117, 118]. As temperature increases, intensity typically decreases due to a shortened phonon lifetime. For the same reason, the mode broadens. The relative intensity of Stokes and anti-Stokes modes is related to the Bose–Einstein distribution, and as such can be used for thermometry. Nonetheless, this feature is not always exploited, due to experimental difficulty in consistent measurements of both Stokes and anti-Stokes peaks. For this reason, most of the thermometry experiments rely on peak position [117].

For the determination of thermal conductivity, the Raman peak position is monitored as a function of the power of the exciting laser. Since absorbed laser energy increases the local temperature, its temperature increases, leading to a shift of the peak position. Thus, comparing the shift per unit of power with the shift per unit of temperature allows the determination of an effective thermal conductance. For the Ge–Ge peak of GeSn and SiGeSn alloys, the shift per unit temperature around room temperature is around $-0.016\ cm^{-1}\ K^{-1}$ [27], and depends on the thermal expansion and anharmonicity, as discussed above.

In these experiments, two configurations of Raman set-up are typically used, with one or two lasers (figures 14(a) and (b)) [117]. In one-laser configuration, heating and probing are obtained with the same laser. In the two-laser case, the probe beam is kept at low power, and the heat is provided by another laser that can be selected with a specific wavelength for high absorption, which can be scanned over the sample for thermal transport imaging [119].

Once the thermal conductance is measured, the conductivity can be extracted, given the sample and beam geometry

[120, 121]. In the simple case of Gaussian beams and a semi-infinite sample, a formula is derived to calculate directly the thermal conductivity, known the beam width [120]. When multiple layers are present, a matrix formalism can be applied [122], but the knowledge of the thicknesses and conductivity of the substrate layers is required, together with numerical evaluation [27, 122]. Using this method, the thermal conductivity for high-quality epitaxial GeSn layers was estimated to be as low as 4 W $(m \cdot K)^{-1}$ for 14 at.% Sn, comparable with measurements with 3ω method (figure 14(c)) [27, 28].

8. Outlook

Raman spectroscopy has become a robust method for the study of SiGeSn alloys, enabling basic characterization, including composition and strain, as well as understanding the atomic structure and properties like anharmonicity and heat transport.

However, the limits and the caveats of the method are nonetheless associated with its fundamental mechanisms. For metrology purposes, a calibration of the spectra is always needed, together with the use of reliable coefficients. The practice suggests that reference samples should be measured together with the sample under investigation, e.g., bulk Ge and GeSn layers of known composition and strain. Comparison of measurements as a function of temperature may be complementary for an even more reliable assessment. When the study of low-intensity peaks is necessary, the highest spectral resolution must be utilized to enable a more reliable deconvolution of the multiple features of the spectra. Here, the use of multiple polarization configurations and two or more excitation wavelengths is beneficial.

Despite the advanced achievements, there are many open fields for the application of Raman spectroscopy to (Si)GeSn.

A more thorough investigation of growth and strain dynamics would be beneficial in developing tailor-made heterostructures for applications in photonics. Typically, Raman spectroscopy is limited to surface analysis because of the poor transparency of the sample. An investigation along the cross-section of the sample is possible with the optical resolution of the microscopy, which is not sufficient for investigations of very thin films of the order of tens of nm or below, as in multi-quantum wells. Here, the use of tip-enhanced Raman spectroscopy (TERS) or other enhancement techniques, coupled with polarization-resolved spectra, will be beneficial. Additionally, this study may utilize NIR/SWIR lasers for excitation, potentially achieving selective resonance with different layers of the heterostructure.

The latter method may also be applied to the study of micro- and nanostructures, which may present peculiar Raman modes associated with symmetry breaking or confinement [123]. These may also be investigated near edges, where 'forbidden' modes can be observed [124, 125].

Raman mapping of microstructures that can be grown by CMOS-compatible methods, together with simulations, can be a platform to investigate peculiar strain configuration (not biaxial) and its spatial distribution [126, 127].

Furthermore, to gain access to the complete quantification of the strain tensor, Raman spectroscopy can make use of non-conventional polarization states, such as 'z-polarization' obtained by radial and azimuthal polarization [128] or high-NA microscopy and off-axis alignment [55, 129, 130].

In the case of mapping, spatial resolution is limited by optics, and submicron resolution is then difficult to achieve. Advanced methods for analysis of hyperspectral images may be applied in this case [82, 131, 132]. The use of photonics enhancement, such as dielectric waveguides [133, 134] or grating-like structures [135], can be considered. TERS is also a path for resolution at the nanoscale [136–138], as well as the enhancement via plasmonic particles [139–141].

Finally, measurement of Raman spectra *in-situ* during growth or etching processes may provide further insight into the growth dynamics in the chemical and mechanical part, i.e., the combination of material formation and strain relaxation. This can be possible in the future by the advancement of optical equipment, e.g., with the realization of high-throughput fiber-based Raman spectroscopes.

Data availability statement

The data that support the findings of this study are available upon reasonable request from the authors.

Acknowledgment

D S acknowledges the grant RYC2022-037186-I by the Spanish MICIU/AEI/10.13039/501100011033 and ESF+. The authors acknowledge financial support from the European Commission for the LASTSTEP project under Grant Agreement No. 101070208, and from the Federal Ministry of Research, Technology and Space (BMFTR) for the GEFORLASER project. G C and D B acknowledge financial support from the German Research Foundation (DFG) under Project No. 537127697 'Thermoelektrische Eigenschaften von SiGeSn-Mikrobauelementen'. Part of this work has been carried out within the Joint Lab 'Intelligent electrooptical sensing' established between IHP and Roma Tre University. C.L.M. acknowledges the ModoMat project (Institutional IHP budget, in the framework of the "IHP junior group Leader" award 2025).

Author contributions

Agnieszka Anna Corley-Wiciak 0000-0003-0974-1190
Conceptualization (supporting), Visualization (equal), Writing – original draft (equal)

Ignatii Zaitsev 0009-0008-9848-8046
Visualization (equal), Writing – review & editing (equal)

Omar Concepción 0000-0001-8197-7523
Writing – review & editing (equal)

Dan Buca 0000-0002-3692-5596
Funding acquisition (equal), Writing – review & editing (equal)

Costanza L Manganelli 0000-0002-4218-2872
Visualization (equal), Writing – original draft (equal), Writing – review & editing (equal)

Giovanni Capellini 0000-0002-5169-2823
Funding acquisition (equal), Supervision (equal), Writing – review & editing (equal)

Davide Spirito 0000-0002-6074-957X
Conceptualization (lead), Funding acquisition (equal), Supervision (equal), Visualization (equal), Writing – original draft (equal), Writing – review & editing (equal)

References

[1] Zheng J, Liu Z, Xue C, Li C, Zuo Y, Cheng B and Wang Q 2018 *J. Semicond.* **39** 061006
[2] Banihashemian S F *et al* 2020 *Opt. Mater. Express* **10** 2242–53
[3] Wirths S, Buca D and Mantl S 2016 *Prog. Cryst. Growth Charact. Mater.* **62** 1–39
[4] Concepción O *et al* 2025 *Adv. Mater.* **37** 2506919
[5] Moutanabbir O *et al* 2021 *Appl. Phys. Lett.* **118** 110502
[6] Grützmacher D, Concepción O, Zhao Q-T and Buca D 2023 *Appl. Phys. A* **129** 235
[7] Elbaz A *et al* 2020 *Nat. Photon.* **14** 375–82
[8] Bouthillier É, Assali S, Nicolas J and Moutanabbir O 2020 *Semicond. Sci. Technol.* **35** 095006
[9] Marzban B *et al* 2023 *ACS Photonics* **10** 217
[10] Fernando N S, Carrasco R A, Hickey R, Hart J, Hazbun R, Schoeche S, Hilfiker J N, Kolodzey J and Zollner S 2018 *J. Vac. Sci. Technol. B* **36** 021202
[11] Reboud V, Buca D, Sigg H, Hartmann J M, Ikonic Z, Pauc N, Calvo V and Chelnokov A 2021 Lasing in group-IV materials *Silicon Photonics IV: Innovative Frontiers* (Springer) p 74
[12] Atalla M R M, Kim Y, Assali S, Burt D, Nam D and Moutanabbir O 2023 *ACS Photonics* **10** 1649–53
[13] Tran H *et al* 2019 *ACS Photonics* **6** 2807–15
[14] Talamas Simola E *et al* 2021 *ACS Photonics* **8** 2166–73
[15] Roucka R, Clark A, Wilson T, Thomas T, Führer M, Ekins-Daukes N, Johnson A, Hoffman R and Begarney D 2016 *IEEE J. Photovolt.* **6** 1025–30
[16] Daligou G, Soref R, Attiaoui A, Hossain J, Atalla M R M, Del Vecchio P and Moutanabbir O 2023 *IEEE J. Photovolt.* **13** 728–35
[17] Roucka R, Mathews J, Beeler R T, Tolle J, Kouvetakis J and Menéndez J 2011 *Appl. Phys. Lett.* **98** 061109
[18] Oehme M, Werner J, Gollhofer M, Schmid M, Kaschel M, Kasper E and Schulze J 2011 *IEEE Photonics Technol. Lett.* **23** 1751–3
[19] Seidel L *et al* 2024 *Nat. Commun.* **15** 10502
[20] Chrétien J *et al* 2019 *ACS Photonics* **6** 2462–9
[21] Wirths S *et al* 2015 *Nat. Photon.* **9** 88–92
[22] Bjelajac A *et al* 2022 *Opt. Express* **30** 3954–61
[23] Liu M *et al* 2023 *Commun. Eng.* **2** 1–9
[24] Tien K, Chen Y, Liu C, Kao H and Li J 2025 *Adv. Electron. Mater.* **11** 2400925
[25] Huang Y-S *et al* 2017 *IEEE Trans. Electron Devices* **64** 2498–504
[26] Kaul P *et al* 2025 *Adv. Electron. Mater.* **11** 2400565
[27] Spirito D, von den Driesch N, Manganelli C L, Zoellner M H, Corley-Wiciak A A, Ikonic Z, Stoica T, Grützmacher D, Buca D and Capellini G 2021 *ACS Appl. Energy Mater.* **4** 7385–92
[28] Concepción O *et al* 2024 *ACS Appl. Energy Mater.* **7** 4394–401
[29] Portavoce A, Khelidj H, Oueldna N, Amhil S, Bertoglio M, Mangelinck D, Essaleh L and Hoummada K 2020 *Materialia* **14** 100873
[30] Zaumseil P, Hou Y, Schubert M A, von den Driesch N, Stange D, Rainko D, Virgilio M, Buca D and Capellini G 2018 *APL Mater.* **6** 076108
[31] Cao B, Chen S, Jin X, Liu J and Li T 2020 *ACS Appl. Mater. Interfaces* **12** 57245–53
[32] Chen S, Jin X, Zhao W and Li T 2024 Phys *Rev. Mater.* **8** 043805
[33] Jin X, Chen S and Li T 2022 *Commun. Mater.* **3** 1–9
[34] Lentz J Z, Woicik J C, Bergschneider M, Davis R, Mehta A, Cho K and McIntyre P C 2023 *Appl. Phys. Lett.* **122** 062103
[35] Gencarelli F, Grandjean D, Shimura Y, Vincent B, Banerjee D, Vantomme A, Vandervorst W, Loo R, Heyns M and Temst K 2015 *J. Appl. Phys.* **117** 095702
[36] Liu S, Covian A C, Wang X, Cline C T, Akey A, Dong W, Yu S-Q and Liu J 2022 *Small Methods* **6** 2200029
[37] Jin X, Chen S, Lemkan C and Li T 2023 *Phys. Rev. Mater.* **7** L111601
[38] Mukherjee M, Srivastava A and Singh A K 2022 *J. Mater. Chem. C* **10** 12524
[39] Giunto A and Fontcuberta I Morral A 2024 *Appl. Phys. Rev.* **11** 041333
[40] Yu P Y and Cardona M 2001 *Fundamentals of Semiconductors: Physics and Materials Properties* (Springer)
[41] Jimenez J and Tomm J W 2016 *Spectroscopic Analysis of Optoelectronic Semiconductors* (Springer)
[42] Corley-Wiciak A A, Concepción O, Zoellner M H, Sfruncia G, Bärwolf F, Nicotra G, Grützmacher D, Buca D, Capellini G and Spirito D 2024 *Phys. Rev. Mater.* **8** 104601
[43] Weinstein B A and Cardona M 1973 *Phys. Rev B* **7** 2545–51
[44] Temple P A 1973 *Phys. Rev. B* **7** 3685–97
[45] D'Costa V R, Tolle J, Poweleit C D, Kouvetakis J and Menéndez J 2007 *Phys. Rev. B* **76** 035211
[46] Renucci M A, Renucci J B, Zeyher R and Cardona M 1974 *Phys. Rev. B* **10** 4309–23
[47] Tomita M, Ogasawara M, Terada T and Watanabe T 2018 *Jpn. J. Appl. Phys.* **57** 04FB04
[48] Pezzoli F *et al* 2008 *Mater. Sci. Semicond. Process.* **11** 279–84
[49] Gurunathan R, Hanus R and Jeffrey Snyder G 2020 *Mater. Horiz.* **7** 1452–6
[50] Khatami S N and Aksamija Z 2016 *Phys. Rev. Appl.* **6** 014015
[51] Gouadec G and Colomban P 2007 *Prog. Cryst. Growth Charact. Mater.* **53** 1–56
[52] Loudon R 1964 *Adv. Phys.* **13** 423–82
[53] Liu X-L, Zhang X, Lin M-L and Tan P-H 2017 *Chin. Phys. B* **26** 067802
[54] Anastassakis E and Cardona M 1998 Phonons, Strains, and Pressure in Semiconductors *Semiconductors and Semimetals* vol 55, ed T Suski and W Paul (*High Pressure in Semiconductor Physics II*) (Elsevier) pp 117–233

[55] Ossikovski R, Nguyen Q, Picardi G, Schreiber J and Morin P 2008 *J. Raman Spectrosc.* **39** 661–72
[56] Ossikovski R, Nguyen Q, Picardi G and Schreiber J 2008 *J. Appl. Phys.* **103** 093525
[57] Takeuchi K, Suda K, Yokogawa R, Usuda K, Sawamoto N and Ogura A 2016 *Jpn. J. Appl. Phys.* **55** 091301
[58] Saltonstall C B, Beechem T E, Amatya J, Floro J, Norris P M and Hopkins P E 2019 *Rev. Sci. Instrum.* **90** 013111
[59] Aspnes D E and Studna A A 1983 *Phys. Rev. B* **27** 985–1009
[60] D'Costa V R, Tolle J, Roucka R, Poweleit C D, Kouvetakis J and Menéndez J 2007 *Solid State Commun.* **144** 240–4
[61] Corley-Wiciak A A, Chen S, Concepción O, Zoellner M H, Grützmacher D, Buca D, Li T, Capellini G and Spirito D 2023 *Phys. Rev. Appl.* **20** 024021
[62] Perova T S, Kasper E, Oehme M, Cherevkov S and Schulze J 2017 *J. Raman Spectrosc.* **48** 993–1001
[63] Nakashima S, Mitani T, Ninomiya M and Matsumoto K 2006 *J. Appl. Phys.* **99** 053512
[64] Pagès O, Souhabi J, Torres V J B, Postnikov A V and Rustagi K C 2012 *Phys. Rev. B* **86** 045201
[65] Picco A, Bonera E, Grilli E, Guzzi M, Giarola M, Mariotto G, Chrastina D and Isella G 2010 *Phys. Rev. B* **82** 115317
[66] Xu C, Wallace P M, Ringwala D A, Chang S L Y, Poweleit C D, Kouvetakis J and Menéndez J 2019 *Appl. Phys. Lett.* **114** 212104
[67] Zhao H, Lin G, Zhang Y, Park S, Hickey R, Zhama T, Cui P, Sourav S, Kolodzey J and Zeng Y 2024 *Opt. Mater.* **149** 114987
[68] Schlipf J *et al* 2021 *J. Raman Spectrosc.* **52** 1167
[69] Talochkin A B, Timofeev V A, Gutakovskii A K and Mashanov V I 2017 *J. Cryst. Growth* **478** 205–11
[70] Fournier-Lupien J-H, Mukherjee S, Wirths S, Pippel E, Hayazawa N, Mussler G, Hartmann J M, Desjardins P, Buca D and Moutanabbir O 2013 *Appl. Phys. Lett.* **103** 263103
[71] Faraci G, Gibilisco S, Russo P, Pennisi A R and La Rosa S 2006 *Phys. Rev. B* **73** 033307
[72] Kumar R and Tanwar M 2021 *J. Raman Spectrosc.* **52** 2100–18
[73] Bagchi S, Poweleit C D, Beeler R T, Kouvetakis J and Menéndez J 2011 *Phys. Rev. B* **84** 193201
[74] Zhang L, Wang Y, Chen N, Lin G, Li C, Huang W, Chen S, Xu J and Wang J 2016 *J. Non-Cryst. Solids* **448** 74–78
[75] Burt D *et al* 2022 *Appl. Phys. Lett.* **120** 202103
[76] Han D, Ye H, Song Y, Zhu Z, Yang Y, Yu Z, Liu Y, Wang S and Di Z 2019 *Appl. Surf. Sci.* **463** 581–6
[77] Raha S, Biswas S, Doherty J, Mondal P K, Holmes J D and Singha A 2022 *Nanoscale* **14** 7211
[78] Cowley J M 1950 *Phys. Rev.* **77** 669–75
[79] Cowley J M 1965 *Phys. Rev.* **138** A1384–9
[80] Rao Y and Curtin W A 2022 *Acta Mater.* **226** 117621
[81] Cao B, Xu E and Li T 2019 *2019 IEEE Photonics Society Summer Topical Meeting Series (SUM)* pp 1–2
[82] Liang Y, West D and Zhang S 2025 *Appl. Phys. Lett.* **126** 202109
[83] Gougam S, De Angelis F, Meneghini C, Concepción O, Buca D, Capellini G and Zoellner M H 2025 *Phys. Rev. Mater.* **9** 064601
[84] Rainko D, Ikonic Z, Vukmirović N, Stange D, von den Driesch N, Grützmacher D and Buca D 2018 *Sci. Rep.* **8** 15557
[85] Wendav T *et al* 2016 *Appl. Phys. Lett.* **108** 242104
[86] Rojas-López M, Navarro-Contreras H, Desjardins P, Gurdal O, Taylor N, Carlsson J R A and Greene J E 1998 *J. Appl. Phys.* **84** 2219–23
[87] Li S F, Bauer M R, Menéndez J and Kouvetakis J 2004 *Appl. Phys. Lett.* **84** 867–9
[88] Su S, Wang W, Cheng B, Hu W, Zhang G, Xue C, Zuo Y and Wang Q 2011 *Solid State Commun.* **151** 647–50
[89] Lin H, Chen R, Huo Y, Kamins T I and Harris J S 2011 *Appl. Phys. Lett.* **98** 261917
[90] Cheng R, Wang W, Gong X, Sun L, Guo P, Hu H, Shen Z, Han G and Yeo Y-C 2013 *ECS J. Solid State Sci. Technol.* **2** 138–45
[91] Oehme M, Buca D, Kostecki K, Wirths S, Holländer B, Kasper E and Schulze J 2013 *J. Cryst. Growth* **384** 71–76
[92] Chang C, Li H, Chen T-P, Tseng W-K, Cheng H, Ko C-T, Hsieh C-Y, Chen M-J and Sun G 2015 *Thin Solid Films* **593** 40–43
[93] Gassenq A *et al* 2017 *Appl. Phys. Lett.* **110** 112101
[94] Vasin A S, Oliveira F, Cerqueira M F, Schulze J and Vasilevskiy M I 2018 *J. Appl. Phys.* **124** 035105
[95] Starman L A, Lott J A, Amer M S, Cowan W D and Busbee J D 2003 *Sens. Actuators A* **104** 107–16
[96] Yang Z, Wang X, Chen W, Tang H, Zhang R, Fan X, Zhang G and Fan J 2024 *Laser Photon. Rev.* **18** 2301300
[97] Tiberj A and Camassel J 2012 Raman imaging in semiconductor physics: applications to microelectronic materials and devices *Raman Imaging* vol 168 (*Springer Series in Optical Sciences*) (Springer) p 46
[98] An S, Tai Y-C, Lee K-C, Shin S-H, Cheng H H, Chang G-E and Kim M 2021 *Nanotechnology* **32** 355704
[99] Burt D, Joo H-J, Jung Y, Kim Y, Chen M, Huang Y-C and Nam D 2021 *Opt. Express* **29** 28959–67
[100] Stange D *et al* 2016 *ACS Photonics* **3** 1279–85
[101] Corley-Wiciak C *et al* 2024 *Small Methods* **8** 2400598
[102] Buca D *et al* 2022 *Adv. Opt. Mater.* **10** 2201024
[103] Süess M J, Minamisawa R A, Geiger R, Bourdelle K K, Sigg H and Spolenak R 2014 *Nano Lett.* **14** 1249–54
[104] Anastassakis E 1997 *J. Appl. Phys.* **82** 1582–91
[105] Burt D *et al* 2017 *Opt. Express* **25** 22911–22
[106] Bard A, Calvo V, Reboud V, Rhun G L, Hartmann J M and Pauc N 2025 *Proc. SPIE* **13371** 154–8
[107] Elbaz A *et al* 2020 *ACS Photonics* **7** 2713–22
[108] Zaitsev I, Corley-Wiciak A A, Corley-Wiciak C, Zoellner M H, Richter C, Zatterin E, Virgilio M, Martín-García B, Spirito D and Manganelli C L 2024 *Phys. Status Solidi RRL* **18** 2300348
[109] Chen M, Joo H-J, Toh E-H, Quek E, Ikonic Z, Du W, Yu S-Q and Nam D 2024 *Proc. SPIE* **13002** 52–55
[110] Li M, Zheng J, Liu X, Zhu Y, Niu C, Pang Y, Liu Z, Zuo Y and Cheng B 2022 *Appl. Phys. Lett.* **120** 121103
[111] Corley-Wiciak A A, Ryzhak D, Zoellner M H, Manganelli C L, Concepción O, Skibitzki O, Grützmacher D, Buca D, Capellini G and Spirito D 2024 *Phys. Rev. Mater.* **8** 023801
[112] Liu T, Miao Y, Wang L, Zhu G, Hu H, Zhong Z, Yang X and Jiang Z 2020 *J. Raman Spectrosc.* **51** 1092–9
[113] Grimvall G 1999 *Thermophysical Properties of Materials* (Elsevier)
[114] Menéndez J and Cardona M 1984 *Phys. Rev. B* **29** 2051–9
[115] Ritz E T, Li S J and Benedek N A 2019 *J. Appl. Phys.* **126** 171102
[116] Manganelli C L, Virgilio M, Skibitzki O, Salvalaglio M, Spirito D, Zaumseil P, Yamamoto Y, Montanari M, Klesse W M and Capellini G 2020 *J. Raman Spectrosc.* **51** 989–96
[117] Sandell S, Chávez-Ángel E, El Sachat A, He J, Sotomayor Torres C M and Maire J 2020 *J. Appl. Phys.* **128** 131101
[118] Kuball M and Pomeroy J W 2016 *IEEE Trans. Device Mater. Reliab.* **16** 667–84
[119] Reparaz J S, Chavez-Angel E, Wagner M R, Graczykowski B, Gomis-Bresco J, Alzina F and Sotomayor Torres C M 2014 *Rev. Sci. Instrum.* **85** 034901
[120] Stoib B, Filser S, Stötzel J, Greppmair A, Petermann N, Wiggers H, Schierning G, Stutzmann M and Brandt M S 2014 *Semicond. Sci. Technol.* **29** 124005

[121] Očenášek J and Voldřich J 2015 *J. Appl. Phys.* **118** 233104
[122] Cahill D G 2004 *Rev. Sci. Instrum.* **75** 5119–22
[123] Tarun A, Hayazawa N, Ishitobi H, Kawata S, Reiche M and Moutanabbir O 2011 *Nano Lett.* **11** 4780–8
[124] Liu T, Lin M-L, Meng D, Cong X, Kan Q, Wu J-B and Tan P-H 2025 *Chin. Phys. B* **34** 017801
[125] Nuytten T, Hantschel T, Kosemura D, Schulze A, De Wolf I and Vandervorst W 2015 *Appl. Phys. Lett.* **106** 033107
[126] Ryzhak D, Corley-Wiciak A A, Steglich P, Yamamoto Y, Frigerio J, Giani R, De Iacovo A, Spirito D and Capellini G 2024 *Mater. Sci. Semicond. Process.* **176** 108308
[127] Ma L, Zheng J, Fan X and Qiu W 2021 *Opt. Express* **29** 30319–26
[128] Saito Y, Kobayashi M, Hiraga D, Fujita K, Kawano S, Smith N I, Inouye Y and Kawata S 2008 *J. Raman Spectrosc.* **39** 1643–8
[129] Kosemura D, Tomita M, Usuda K and Ogur A 2012 Stress measurements in Si and SiGe by liquid-immersion Raman spectroscopy *Advanced Aspects of Spectroscopy* ed M Akhyar Farrukh (InTech)
[130] Khan Z, Nuytten T, Favia P, Fleischmann C, De Wolf I and Vandervorst W 2022 *J. Appl. Phys.* **132** 035104
[131] Duponchel L, Milanfar P, Ruckebusch C and Huvenne J-P 2008 *Anal. Chim. Acta* **607** 168–75
[132] Tipping W J, Faulds K and Graham D 2024 *Chem. Biomed. Imaging* **2** 733–43
[133] Poborchii V, Tada T and Kanayama T 2009 *Appl. Phys. Lett.* **94** 131907
[134] Nuytten T, Bogdanowicz J, Hantschel T, Schulze A, Favia P, Bender H, Wolf I D and Vandervorst W 2017 *Adv. Eng. Mater.* **19** 1600612
[135] Nuytten T, Bogdanowicz J, Sergeant S and Fleischmann C 2024 *Appl. Phys. Lett.* **125** 053506
[136] Nuytten T, Bogdanowicz J, Witters L, Eneman G, Hantschel T, Schulze A, Favia P, Bender H, De Wolf I and Vandervorst W 2018 *APL Mater.* **6** 058501
[137] Vanacore G M *et al* 2013 *Phys. Rev. B* **88** 115309
[138] Hermann P, Hecker M, Chumakov D, Weisheit M, Rinderknecht J, Shelaev A, Dorozhkin P and Eng L M 2011 *Ultramicroscopy* **111** 1630–5
[139] Ma X, Zhu Y, Yu N, Kim S, Liu Q, Apontti L, Xu D, Yan R and Liu M 2019 *Nano Lett.* **19** 100–7
[140] Hashiguchi H, Takei M, Kosemura D and Ogura A 2012 *Appl. Phys. Lett.* **101** 172101
[141] Kasim J, Tee X Y, You Y M, Ni Z H, Setiawan Y, Lee P S, Chan L and Shen Z X 2008 *J. Raman Spectrosc.* **39** 1338–42